

# Neural Backward Filtering Forward Guiding

Gefan Yang<sup>1</sup> Frank van der Meulen<sup>2</sup> Stefan Sommer<sup>1</sup>

## Abstract

Inference in non-linear continuous stochastic processes on trees is challenging, particularly when observations are sparse (leaf-only) and the topology is complex. Exact smoothing via Doob’s  $h$ -transform is intractable for general non-linear dynamics, while particle-based methods degrade in high dimensions. We propose Neural Backward Filtering Forward Guiding (NBFFG), a unified framework for both discrete transitions and continuous diffusions. Our method constructs a variational posterior by leveraging an auxiliary linear-Gaussian process. This auxiliary process yields a closed-form backward filter that serves as a “guide”, steering the generative path toward high-likelihood regions. We then learn a neural residual—parameterized as a normalizing flow or a controlled SDE—to capture the non-linear discrepancies. This formulation allows for an unbiased path-wise subsampling scheme, reducing the training complexity from tree-size dependent to path-length dependent. Empirical results show that NBFFG outperforms baselines on synthetic benchmarks, and we demonstrate the method on a high-dimensional inference task in phylogenetic analysis with reconstruction of ancestral butterfly wing shapes.

## 1. Introduction

Stochastic processes defined on tree structures are fundamental for modeling hierarchical dependencies in complex systems. Applications range from tracing phylogenetic evolution in biology (Felsenstein, 1981; Huelsenbeck et al., 2003), modeling the state spaces of spin glasses in statistical physics(Bovier, 2017), to analyzing cascading diffusion in social networks(Kempe et al., 2003). In these settings, a

central inferential challenge is the smoothing problem: reconstructing the latent trajectories of internal hidden states given partially available observations, e.g., only at leaves or final outcomes. Theoretically, exact Bayesian inference in this context is characterized by Doob’s  $h$ -transform, which conditions the generative process on future observations via a harmonic  $h$ -function. Computing this  $h$ -function can be done by “collecting evidence” or “passing messages” from leaves to the root, which yields the concept of “belief propagation” or “sum-product message passing”. While this backward pass is analytically tractable for simple Linear-Gaussian models, it becomes computationally prohibitive for general non-linear dynamics.

Current approaches to this intractable problem often rely on stochastic simulation methods like Sequential Monte Carlo (SMC) or Markov Chain Monte Carlo (MCMC). However, particle-based methods suffer from weight degeneracy, particularly for the smoothing problem and as the hierarchy deepens. MCMC schemes may face prohibitive mixing times in deep trees because the vanishing information signal between the root and distant leaves results in a nearly flat posterior surface, forcing the sampler into an inefficient random walk across a vast state space. To overcome these limitations, we introduce Neural Backward Filtering Forward Guiding (NBFFG), a deep variational framework that amortizes the cost of inference. Our core insight is to approximate the intractable posterior by “warm-starting” it with a tractable proxy. We first construct a guided process where Doob’s  $h$ -transform is replaced by a computationally cheap approximation. This acts as a coarse “guide”, steering the generative process towards high-likelihood regions. We then learn a neural residual—parameterized as a normalizing flow or controlled stochastic differential equation (SDE) to capture the fine-grained non-linear discrepancies, significantly reducing the complexity compared to learning the full dynamics from scratch.

Our contributions are summarized as follows:

- We propose a novel method for smoothing both discrete and continuous processes on directed trees, combining analytical linear guidance with learnable neural residuals to ensure robust inference across diverse dynamics.
- We introduce a path-wise subsampling scheme and a

transductive amortization strategy. This reduces training costs from tree size to path size, and allows a single shared network to generalize across deep hierarchies.

- We demonstrate the method’s versatility by recovering analytical ground truths in linear models, resolving mode collapse in multimodal non-linear systems where baseline methods are challenged, and successfully reconstructing high-dimensional ancestral butterfly morphologies in a real-world phylogenetic application.

## 2. Related Work

**Smoothing of state-space models** For Linear Gaussian State-space Model (LG-SSM), the Kalman smoother, also known as the Rauch-Tung-Striebel (RTS) smoother (Rauch et al., 1965) yields exact marginal smoothing distributions via a forward-backward recursion, see for instance, (Sarkka, 2023)[Chapter 12]. Sampling from the smoothing distribution in LG-SSMs is achieved by forward filtering-backward sampling, introduced firstly by (Carter & Kohn, 1994) and (Frühwirth-Schnatter, 1994). (Pearl, 1988) generalized this forward-backward recursions to a tree, which is known as “belief propagation” or “sum-product message passing”. This algorithm consists of a backward “collect evidence” phase and a subsequent forward “distribute evidence” phase. Extensions to richer tree models include (Chou et al., 1994; Bardel & Desbouvries, 2012; Desbouvries et al., 2006).

**Sampling methods** Particle-based methods offer a robust framework for inference in nonlinear, non-Gaussian models. Briers et al. (2010) established a principled two-filter smoothing formulation, while Whiteley (2014) introduced “twisting” to mitigate weight degeneracy. Subsequent works have refined this by iteratively approximating optimal twists (Guarniero et al., 2017) or framing twisting as a stochastic control problem (Heng et al., 2020). Recently, learning-based approaches have integrated neural networks to approximate optimal proposals and Doob’s  $h$ -transforms (Paige & Wood, 2016; Chopin et al., 2023). Notably, methods like SI $\chi$ O and NAS- $\chi$  embed SMC into reweighted wake-sleep objectives to achieve low-variance gradient estimation (Lawson et al., 2022; 2023).

**Smoothing of diffusions** Also known as the diffusion bridge problem, this task is commonly addressed via Monte Carlo sampling using “guided proposals” (Delyon & Hu, 2006; Schauer et al., 2017), a concept recently extended to directed acyclic graphs (DAGs) by (van der Meulen & Sommer, 2026). Alternatively, learning-based methods employ techniques such as score matching (Heng et al., 2025), adjoint processes (Baker et al., 2025), self-consistency objectives (Howard et al., 2025), or neural guidance (Yang, 2025). Our work builds directly upon (van der Meulen & Sommer, 2026), which formulates the proposal distribution

over tree topologies, and (Yang, 2025), which introduces a learnable objective for approximating the posterior. We unify and extend these frameworks to enable scalable, high-dimensional inference on complex tree structures.

## 3. Preliminaries

### 3.1. Probabilistic models on tree diagrams

Let  $\mathcal{G} = (\mathcal{V}, \mathcal{E})$  be a directed rooted tree with vertex set  $\mathcal{V}$  and edge set  $\mathcal{E}$ . The set  $\mathcal{V}$  contains a distinct fixed root  $\mathbf{0}$  and a set of non-root vertices  $\mathcal{V}^+ := \mathcal{V} \setminus \{\mathbf{0}\}$ . For any vertex  $v$ , let  $\text{pa}(v)$  and  $\text{ch}(v)$  denote the parent and the set of children of  $v$ , respectively (if existent). Since  $\mathcal{G}$  is a tree rooted at  $\mathbf{0}$ , every vertex  $v \in \mathcal{V}^+$  has exactly one parent, while  $\text{pa}(\mathbf{0}) = \emptyset$ .

We denote a directed edge from  $\text{pa}(v)$  to  $v$  as  $(\text{pa}(v), v) \in \mathcal{E}$ . The notation  $u \rightsquigarrow v$  indicates that  $v$  is reachable from  $u \in \mathcal{V}$  (including the case  $u = v$ ). Let  $\mathcal{L} \subset \mathcal{V}$  denote the set of leaves (vertices without children). For a vertex  $v$ , we define the set of descendant leaves  $\mathcal{L}_v$  as  $\mathcal{L}_v := \{l \in \mathcal{L} : v \rightsquigarrow l\}$ .

We consider a generative model defined on a directed tree  $\mathcal{G} = (\mathcal{V}, \mathcal{E})$  rooted at  $\mathbf{0}$ . To each vertex  $v \in \mathcal{V}$ , a continuous random vector  $X_v$  taking values in  $\mathbb{R}^d$  is associated.

We adopt a structural assumption that, given the state of  $v$ , the states of its children  $\text{ch}(v)$  evolve independently. If the root is fixed as  $X_0 = x_0$ , consequently, the joint law  $\mathbb{P}$  of the system factorizes over the edges of the tree:

$$\mathbb{P}(\mathrm{d}X_{\mathcal{V}^+}) = \prod_{v \in \mathcal{V}^+} \mathbb{P}_v(\mathrm{d}X_v \mid X_{\text{pa}(v)}), \quad (1)$$

The edge-wise conditional law  $\mathbb{P}_v$  describes the forward transitional evolution along the edge  $(\text{pa}(v), v)$ . We distinguish between two types of edge dynamics—discrete steps and continuous paths—formulated via Markov transition kernels and path measures, respectively.

**Definition 3.1.** An edge  $(\text{pa}(v), v) \in \mathcal{E}$  is *discrete* if the transition implies a direct time-step. The dependence of  $X_v$  on  $X_{\text{pa}(v)}$  is specified by a Markov transition kernel  $P_v(x, \mathrm{d}x') \equiv \mathbb{P}_v(X_v \in \mathrm{d}x' \mid X_{\text{pa}(v)} = x)$  defined on  $(\mathbb{R}^d, \mathcal{B}(\mathbb{R}^d))$ . We also assume this kernel admits a strictly positive density  $p_v(x' \mid x)$  with respect to the Lebesgue measure  $P_v(x, \mathrm{d}x') = p_v(x' \mid x) \mathrm{d}x'$ .

Throughout the paper, we specialize to the following Gaussian transition kernel defined by:

$$P_v(x, \mathrm{d}x') = \varphi(x'; \mu(x), \Sigma(x)) \mathrm{d}x', \quad (2)$$

where  $\varphi(y; \mu, \Sigma)$  denotes the density function of a Gaussian distribution  $\mathcal{N}(\mu, \Sigma)$  with mean  $\mu$  and covariance  $\Sigma$ , evaluated at  $y$ . The maps  $x \mapsto \mu(x) \in \mathbb{R}^d, x \mapsto \Sigma(x) \in \mathbb{S}_+^d$  denote the mean and covariance function, respectively.

**Definition 3.2.** An edge  $(\text{pa}(v), v) \in \mathcal{E}$  is *continuous* if it represents a diffusion process over a time interval  $[0, T_v]$ . Let  $(C([0, T_v], \mathbb{R}^d), \{\mathcal{F}_t\}, \mathbb{P}_v)$  be a filtered probabilistic path space. The dynamics are governed by the SDE:

$$dZ_v(t) = b(Z_v(t))dt + \sigma(Z_v(t))dW_t^{\mathbb{P}_v}, \quad (3)$$

associated with the path measure  $\mathbb{P}_v$  under standard Lipschitz conditions on  $b$  and  $\sigma$ , such that  $Z_v(0) = X_{\text{pa}(v)} = x \in \mathbb{R}^d$  almost surely. The conditional probability of the child state  $X_v$  is the marginal at the terminal time  $t = T_v$ :  $\mathbb{P}_v(X_v \in dx' | X_{\text{pa}(v)} = x) = \mathbb{P}_v(Z_v(T_v) \in dx')$ .

At the leaves  $\mathcal{L}$ , the states  $X_{\mathcal{L}} = \{X_l\}_{l \in \mathcal{L}}$  are observed with a known observation model  $\mathbb{L}(Y | X)$  which has a density  $\ell(y | x)$  with respect to the Lebesgue measure in  $\mathbb{R}^d$ . Given the observations at leaves, our goal is to find a variational approximation to the generally intractable posterior distribution of the internal vertices, i.e., the smoothing distribution  $\Pi$ .

### 3.2. Doob's $h$ -transform

Exact Bayesian inference on the tree requires conditioning the generative process on the observations at the leaves  $\mathcal{L}$ . This conditioning can be realized through Doob's  $h$ -transform (see e.g., (van der Meulen & Sommer, 2026)[Section 3]), which constructs the posterior process by re-weighting the prior dynamics with a harmonic  $h$ -function that encapsulates future observations.

**Discrete dynamics** Let  $h_v(x)$  denote the density of  $Y_{\mathcal{L}_v}$  (the observations of  $X_{\mathcal{L}_v}$ ) conditioned on  $\{X_v = x\}$ . For a discrete edge  $(\text{pa}(v), v)$ , the posterior transition kernel  $\Pi_v(x, dx')$  relates to the prior kernel  $P_v(x, dx')$  via:

$$\Pi_v(x, dx') = \frac{h_v(x')}{h_{\text{pa}(v), v}(x)} P_v(x, dx'), \quad (4)$$

where  $h_{\text{pa}(v), v}(x) := \int h_v(x') P_v(x, dx')$ .

**Continuous dynamics** Let  $h_v(t, z)$  denote the density of  $Y_{\mathcal{L}_v}$  conditioned on  $\{Z_v(t) = z\}$ . For a continuous edge  $(\text{pa}(v), v)$ , the posterior dynamics are characterized by a change of measure, defined by

$$\frac{d\Pi_v}{d\mathbb{P}_v} \Big|_{\mathcal{F}_t} = \frac{h_v(t, Z_v(t))}{h_v(0, Z_v(0))}, \quad \forall t \in [0, T_v]. \quad (5)$$

By Girsanov's theorem, it follows that the posterior dynamics are governed by the SDE:

$$\begin{aligned} dZ_v(t) &= b(Z_v(t))dt + \sigma(Z_v(t))dW_t^{\Pi_v} \\ &+ \Sigma(Z_v(t))\nabla \log h_v(t, Z_v(t))dt, \end{aligned} \quad (6)$$

where  $\Sigma(z) := \sigma(z)\sigma(z)^\top$ , and  $W_t^{\Pi_v}$  is a  $\Pi_v$ -Wiener process. Equation (6) is also known as the diffusion bridge SDE.

With the edge-wise posteriors transformed by  $h$ -functions, we can now formally define the smoothing distribution as the joint posterior law:

$$\Pi(dX_{\mathcal{V}}) := \prod_{v \in \mathcal{V}^+} \Pi_v(dX_v | X_{\text{pa}(v)}), \quad (7)$$

which directly follows the prior definition Equation (1).

### 3.3. Backward information filter

Determining the  $h$ -functions requires a recursive procedure known as the *backward information filter (BIF)*, see for instance (Felsenstein, 1981; Briers et al., 2010; Guarnerio et al., 2017; Heng et al., 2020). Due to the conditional independence of branches rooted at a vertex  $v$ , we have

$$h_v(x) = \prod_{c \in \text{ch}(v)} h_{v,c}(x), \quad (8)$$

where  $h_{v,c}(x) := \mathbb{E}_{\mathbb{P}_c}[h_c(X_c) | X_v = x]$  is the expectation of the  $h$ -function at child  $c$ , conditioned on  $\{X_v = x\}$ . For leaf vertices  $l \in \mathcal{L}$  without children,  $h_l$  is directly initialized as the likelihood density of the leaf observation:  $h_l(x) = \ell(y_l | x)$ , where  $y_l$  is the observed realization of the leaf state  $X_l$ .

The evaluation of the expectations  $\mathbb{E}_{\mathbb{P}_c}[h_c(X_c) | X_v = x]$  differs fundamentally depending on the edge dynamics. For a discrete edge, the expectation is directly obtained by:

$$\mathbb{E}_{\mathbb{P}_c}[h_c(X_c) | X_v = x] = \int h_c(x') P_c(x, dx'). \quad (9)$$

For a continuous edge defined over  $t \in [0, T_c]$ , if we define  $\psi(t, z) = \mathbb{E}_{\mathbb{P}_c}[h_c(Z_v(T_c)) | Z_v(t) = z]$ , then by the Feynman-Kac formula,  $\psi$  satisfies the Kolmogorov backward equation:

$$\left( \frac{\partial}{\partial t} + \mathcal{A} \right) \psi(t, z) = 0, \quad \psi(T_c, z) = h_c(z), \quad (10)$$

where  $\mathcal{A}$  is the infinitesimal generator of the diffusion, i.e., for vector field  $f: \mathbb{R}^d \rightarrow \mathbb{R}^d$ ,  $\mathcal{A}f(x) = \sum_i b_i(x)\partial_i f(x) + \frac{1}{2} \sum_{i,j} (\sigma\sigma^\top)_{i,j}(x)\partial_{i,j} f(x)$ . Then the expectation is the solution of Equation (10) at the initial time  $t = 0$ :  $\mathbb{E}_{\mathbb{P}^c}[h_c(X_c) | X_v = x] = \psi(0, x)$ .

While the  $h$ -transform provides a rigorous probabilistic solution, the exact BIF is generally computationally intractable. Analytically solving either Equation (9) or Equation (10) can be nontrivial for nonlinear prior transitions or SDEs, which motivates the variational approximation proposed in the subsequent section.

## 4. Methodology

Our approach constructs a variational posterior that approximates the exact posterior distributions discussed previously.

For general non-linear models, we decompose the inference task into two components: a coarse-grained linear approximation that provides rough guidance, and a fine-grained neural parameterization that captures nonlinear statistics.

#### 4.1. Guided proposal

We first recall key results from (van der Meulen & Sommer, 2026), which establish that if the edge transitions are linear Gaussian, the BIF admits a closed-form solution. Specifically, for discrete edges, we consider transitions of the form:

$$P_v(x, dx') = \varphi(x'; Bx + \beta, \tilde{\Sigma}), \quad (11)$$

and for continuous edges, transitions governed by SDE:

$$dZ_v(t) = [B(t)Z_v(t) + \beta(t)]dt + \tilde{\sigma}(t)dW_t. \quad (12)$$

Under these conditions, for any vertex  $v$ , the  $h$ -functions take the canonical Gaussian forms:

$$\text{discrete: } \log h_v(x) = -\frac{1}{2}x^\top Hx + \eta^\top x + C,$$

$$\text{continuous: } \log h_v(t, z) = -\frac{1}{2}z^\top H(t)z + \eta(t)^\top z + C,$$

where  $H \in \mathbb{S}_+^d$  (or  $H : [0, T_v] \rightarrow \mathbb{S}_+^d$ ) is the precision matrix (function) and  $\eta \in \mathbb{R}^d$  (or  $\eta : [0, T_v] \rightarrow \mathbb{R}^d$ ) is the information vector (function). Since exact  $h$ -functions are intractable for general non-linear models, (van der Meulen & Sommer, 2026) propose approximating the dynamics with auxiliary linear Gaussian processes (following Equation (11) or Equation (12)). The resulting analytically tractable  $h$ -functions, denoted as  $\tilde{h}$ , serve as proxies for the true  $h$ . Substituting  $h$  with  $\tilde{h}$  yields an approximate posterior known as the *guided proposal*. This framework, termed Backward Filtering Forward Guiding (BFFG), was originally developed to generate efficient proposals for MCMC, and here serves as the foundation for our variational method. Details of the guided proposal are provided in Section A.1.

#### 4.2. Variational posterior

Directly employing the BIF presents a practical challenge: optimally selecting the linear parameters triplet— $(B, \beta, \tilde{\Sigma})$  for discrete edges or  $(B, \beta, \tilde{\sigma})$  for continuous ones—is often intractable in general non-linear settings. While some strategies for triplet selection exist (Mider et al., 2021), we propose an alternative approach. We begin with a simplified auxiliary construction (e.g., ignoring drift by setting  $B \equiv 0, \beta \equiv 0$ ) to derive a computationally tractable approximation, the BIF proxy  $\tilde{h}$ . While this proxy captures the conditional structure imposed by observations, it may inevitably ignore non-linearities. To bridge this gap, we introduce a learnable variational posterior,  $\mathbb{Q}_v$ , specifically designed to remedy the deficiencies of the coarse linear guidance.

Formally,  $\mathbb{Q}_v$  is defined on the same measurable space as the prior  $\mathbb{P}_v$ : specifically,  $(\mathbb{R}^d, \mathfrak{B}(\mathbb{R}^d))$  for discrete transitions or  $(C([0, T_v], \mathbb{R}^d), \{\mathcal{F}_t\})$  for continuous paths. Crucially, rather than defining  $\mathbb{Q}_v$  via a direct change of measure on the unconditioned prior  $\mathbb{P}_v$  (as discussed in Section 3.2), we construct it by transforming the guided proposal induced by  $\tilde{h}$  using a parameterized neural model (e.g., a normalizing flow or a neural SDE). In this framework, the variational distribution incorporates the coarse guidance from  $\tilde{h}$  by design, leaving the neural component to learn only the remaining discrepancy required to recover the true non-linear posterior.

**Discrete dynamics** Consider a discrete edge  $(\text{pa}(v), v)$ , whose dynamics is modeled by the transition kernel  $P_v(x, dx')$ . Following Equation (4), we first construct a guided proposal kernel  $\tilde{\Pi}_v$  by reweighting the prior transition  $P_v$  with the proxy  $\tilde{h}_v$  instead of  $h_v$ :

$$\tilde{\Pi}_v(x, dx') := \frac{\tilde{h}_v(x')}{\tilde{h}_{\text{pa}(v), v}(x)} P_v(x, dx'), \quad (14)$$

where  $\tilde{h}_{\text{pa}(v), v}(x) := \int \tilde{h}_v(x') P_v(x, dx')$ . Although the exact posterior transition kernel  $\Pi_v$  is intractable, this guided proposal provides a closed-form, analytic base distribution by exploiting the linear structure of the auxiliary system.

As discussed, to capture non-linear dependencies missed by the approximate guidance, we define a parameterized variational posterior transition kernel  $\mathbb{Q}_v^\theta$  as the pushforward of  $\tilde{\Pi}_v$  via a parameterized diffeomorphism  $F_v^\theta : \mathbb{R}^d \rightarrow \mathbb{R}^d$  (i.e., a normalizing flow). Formally,  $\mathbb{Q}_v^\theta(\cdot | x) = (F_v^\theta)_\# \tilde{\Pi}_v(\cdot | x)$ . Here, we assume that both  $\tilde{\Pi}_v$  and  $\mathbb{Q}_v^\theta$  admit densities  $\tilde{\pi}_v$  and  $q_v^\theta$  with respect to the Lebesgue measure in  $\mathbb{R}^d$ .  $q_v^\theta$  can then be computed via the change of variables formula:

$$\log q_v^\theta(x' | x) = \log \tilde{\pi}_v(x' | x) - \log |\det J_{F_v^\theta}(\tilde{x}')|, \quad (15)$$

where  $\tilde{x}' = (F_v^\theta)^{-1}(x')$ , and  $J_{F_v^\theta}$  is the Jacobian of  $F_v^\theta$  with respect to  $\tilde{x}'$ .

**Continuous dynamics** Unlike the discrete case, the posterior distribution of a continuous edge  $(\text{pa}(v), v)$  is modeled by a path measure  $\Pi_v$ , induced by the SDE Equation (6). To approximate the path measure on the space  $C([0, T_v], \mathbb{R}^d)$ . We construct a variational path measure  $\mathbb{Q}_v^\theta$  via a parameterized Girsanov transformation. We first define a vector field  $g_v^\theta$  that decomposes into the score (i.e., the gradient of the logarithm) of the tractable proxy  $\tilde{h}_v$  and a learnable neural vector field  $s_v^\theta : [0, T_v] \times \mathbb{R}^d \rightarrow \mathbb{R}^d$ . Specifically,  $g_v^\theta(t, z) := \nabla \log \tilde{h}_v(t, z) + s_v^\theta(t, z)$ . Then the variational path measure  $\mathbb{Q}_v^\theta$  is defined by the Radon-Nikodym derivative  $d\mathbb{Q}_v^\theta = M_v(T_v) d\mathbb{P}_v$ , where  $M_v(t)$  is a martingale:

$$M_v(t) := \exp \left( \int_0^t g_v^\theta(u, Z_v(u))^\top \sigma(Z_v(u)) dW_u^{\mathbb{P}_v} - \frac{1}{2} \int_0^t \|g_v^\theta(u, Z_v(u))\|_{\Sigma(Z_v(u))}^2 du \right), \quad (16)$$

where  $\|v\|_A^2 := v^\top A v$ . By Girsanov's theorem, under  $\mathbb{Q}_v^\theta$ , the process  $Z_t$  evolves according to the SDE:

$$\begin{aligned} dZ_v(t) &= b(Z_v(t))dt + \sigma(Z_v(t))dW_t^{\mathbb{Q}_v^\theta} \\ &+ \Sigma(Z_v(t))g_v^\theta(t, Z_v(t))dt, \end{aligned} \quad (17)$$

where  $W^{\mathbb{Q}_v^\theta}$  is a standard Wiener process under  $\mathbb{Q}_v^\theta$ .

**Root inference** One may also want to infer the root posterior by assigning a prior  $\mathbb{P}_0$  on the root instead of fixing it. This can be done by augmenting the tree with a virtual root  $-1$  and a directed edge  $(-1, 0)$ , effectively treating the prior  $\mathbb{P}_0$  as a conditional transition. We can then fix the state of the virtual root to be a suitable constant  $x_{-1}$  and define the transition of the edge  $(-1, 0)$  such that its marginal recovers the required root prior:  $\mathbb{P}_0(\cdot | x_{-1}) := \mathbb{P}_0(\cdot)$ . For instance, under the Gaussian prior  $\mathbb{P}_0$ , it corresponds to a linear transition. This allows the application of the edge-wise variational definition to the actual root without modification. Without loss of generality, we always denote  $0$  as the fixed root, whether it is the actual or virtual root.

### 4.3. Loss function

Providing the constructed edge-wise variational posteriors, we now aim to optimize them by variational inference. Specifically, we first define a joint variational law  $\mathbb{Q}^\theta$  of the whole system in a similar way as  $\Pi$ :

$$\mathbb{Q}^\theta(dX_{\mathcal{V}^+}) := \prod_{v \in \mathcal{V}^+} \mathbb{Q}_v^\theta(dX_v | X_{\text{pa}(v)}). \quad (18)$$

The goal is to approximate the exact posterior  $\Pi$  with  $\mathbb{Q}^\theta$ . We achieve this by minimizing the Kullback-Leibler (KL) divergence  $D_{\text{KL}}(\mathbb{Q}^\theta \| \Pi)$ , which is equivalent to minimizing the negative global Evidence Lower Bound (ELBO).

**Theorem 4.1.** *Assume that for each  $v \in \mathcal{V}^+$ ,  $\mathbb{Q}_v^\theta$  is absolutely continuous with respect to  $\mathbb{P}_v$ . For each leaf  $l \in \mathcal{L}$ , let  $y_l$  be the observed realization of the leaf state  $X_l$ , characterized by the conditional likelihood density  $\ell(y_l | X_l)$ . The loss function is defined as the negative ELBO, which decomposes as follows:*

$$\mathcal{J}(\theta) = \sum_{v \in \mathcal{V}^+} D_{\text{KL}}(\mathbb{Q}_v^\theta \| \mathbb{P}_v) - \sum_{l \in \mathcal{L}} \mathbb{E}_{\mathbb{Q}_l^\theta} [\log \ell(y_l | X_l)]. \quad (19)$$

Then  $\mathcal{J}(\theta) = D_{\text{KL}}(\mathbb{Q}^\theta \| \Pi) - C$ , with  $C = \log h_0(x_0)$  as a  $\theta$ -independent constant to optimization.

Therefore,  $\mathcal{J}(\theta)$  is lower bounded by  $-\log h_0(x_0)$ . The evaluation of  $D_{\text{KL}}(\mathbb{Q}_v^\theta \| \mathbb{P}_v)$  can vary from discrete to continuous edges. We then specialize in two different edge dynamics to derive the computable forms of  $\mathcal{J}(\theta)$ .

**Discrete dynamics** Recall that we formulate the variational posterior as a parameterized pushforward of the guided proposal:  $\mathbb{Q}_v^\theta := (F_v^\theta)_\# \tilde{\Pi}_v$ . In this case, we can compute  $\mathcal{J}(\theta)$  according to the following corollary.

**Corollary 4.2.** *Let  $F_v^\theta : \mathbb{R}^d \rightarrow \mathbb{R}^d$  be a diffeomorphism with Jacobian  $J_{F_v^\theta}$ , then*

$$\begin{aligned} \mathcal{J}(\theta) &= \sum_{v \in \mathcal{V}^+} \mathbb{E} \left[ \log \frac{\tilde{\pi}_v(\tilde{X}_v | X_{\text{pa}(v)})}{p_v(X_v^\theta | X_{\text{pa}(v)})} \right] \\ &- \sum_{v \in \mathcal{V}} \mathbb{E} \left[ \log \left| \det J_{F_v^\theta}(\tilde{X}_v) \right| \right] \\ &- \sum_{l \in \mathcal{L}} \mathbb{E} [\log \ell(y_l | X_l^\theta)], \end{aligned} \quad (20)$$

where  $X_v^\theta = F_v^\theta(\tilde{X}_v)$ , i.e., the transformed sample at  $v$ . The expectations are taken over  $X_{\text{pa}(v)} \sim \mathbb{Q}_{\text{pa}(v)}^\theta$ ,  $\tilde{X}_v \sim \tilde{\Pi}_v(\cdot | X_{\text{pa}(v)})$ .

**Continuous dynamics** For continuous edges,  $\mathcal{J}(\theta)$  can be computed by the following corollary.

**Corollary 4.3.** *Let  $s_v^\theta$  be bounded and the map  $z \mapsto s_v^\theta(t, z)$  be Lipschitz continuous, and  $g_v^\theta(t, z) := \nabla \log \tilde{h}_v(t, z) + s_v^\theta(t, z)$ , then*

$$\begin{aligned} \mathcal{J}(\theta) &= \sum_{v \in \mathcal{V}^+} \frac{1}{2} \mathbb{E} \left[ \int_0^{T_v} \|g_v^\theta(t, Z_v(t))\|_{\Sigma(Z_v(t))}^2 dt \right] \\ &- \sum_{l \in \mathcal{L}} \mathbb{E} [\log \ell(y_l | Z_v(T_l))], \end{aligned} \quad (21)$$

where the expectations are taken over  $Z_v \sim \mathbb{Q}_v^\theta(\cdot | X_{\text{pa}(v)})$ , and  $X_{\text{pa}(v)} = Z_v(T_{\text{pa}(v)})$ .

**Subsampling** Evaluating  $\mathcal{J}(\theta)$  requires accumulating edge-wise KL divergences  $D_{\text{KL}}(\mathbb{Q}_v^\theta \| \mathbb{P}_v)$  for all  $v \in \mathcal{V}^+$ . Direct optimizing over the whole tree can be nontrivial, since the gradients need to be computed and backpropagated through every edge. However, we can mitigate this issue by applying a subsampling scheme, where instead of sampling for all  $v \in \mathcal{V}^+$ , we estimate the loss by sampling only along a certain root-to-leaf path at each iteration. The following proposition shows that such single-path estimation can be an unbiased estimator of the full-tree loss.

**Proposition 4.4.** *Suppose a leaf  $l \in \mathcal{L}$  is selected with probability  $\gamma(l)$ . Let  $\mathcal{V}_l^+ \subseteq \mathcal{V}^+$  denote the set of vertices on the unique path  $0 \rightsquigarrow l$ . Define the edge selection probability  $\omega(v)$  as:*

$$\omega(v) := \sum_{l \in \mathcal{L}_v} \gamma(l) = \sum_{l \in \mathcal{L}} \gamma(l) \mathbb{1}(v \in \mathcal{V}_l^+), \quad (22)$$

where  $\mathcal{L}_v$  is the set of leaves in the subtree of  $v$ ,  $\mathbb{1}$  is the indicator function. Then the path loss:

$$\mathcal{J}'_l(\theta) = \sum_{v \in \mathcal{V}_l^+} \frac{D_{\text{KL}}(\mathbb{Q}_v^\theta \| \mathbb{P}_v)}{\omega(v)} - \frac{\log \ell(y_l | X_l)}{\gamma(l)} \quad (23)$$

is an unbiased estimator of the full-tree loss:

$$\mathcal{J}(\theta) = \sum_{v \in \mathcal{V}^+} D_{\text{KL}}(\mathbb{Q}_v^\theta \| \mathbb{P}_v) - \sum_{l \in \mathcal{L}} \log \ell(y_l | X_l). \quad (24)$$

This is a helpful result as it can restrict the size of the computation graph from the whole tree  $\mathcal{V}$  into a single path  $\mathbf{0} \rightsquigarrow l$ . A simple choice consists of selecting a leaf uniformly from the set of leaf vertices. This leads to  $\gamma(l) = 1/|\mathcal{L}|$  and  $\omega(v) = |\mathcal{L}_v|/|\mathcal{L}|$ . Naturally, subsampling can be applied to both Equation (20) and Equation (21) for significantly reducing computational cost.

This concludes the construction of our framework, which operates in two phases. First, in the *Backward Filtering* phase, we compute the closed-form proxy  $\tilde{h}$  using a pre-defined linear auxiliary process. Second, in the *Neural Forward Guiding* phase, we combine this proxy with a learnable neural component to define the variational posterior process, effectively steering the generative trajectory toward the observations. We term this unified framework *Neural Backward Filtering Forward Guiding (NBFFG)*.

#### 4.4. Amortized learning

To scale to large tree structures, optimizing separate variational parameters for every vertex is computationally prohibitive. We address this via intra-tree amortization, where a single shared network  $\theta$  approximates the posterior transitions for all edges in the topology.

To distinguish between different lineages while maintaining parameter efficiency, we condition the network on a learnable embedding  $c_v$  for each vertex index. This formulation is transductive: the network is specialized to the training topology. This allows the model to pool information across similar branches (e.g., siblings with similar observations) and drastically reduces the parameter space compared to independent variational inference, though it requires retraining or fine-tuning to adapt to new tree structures.

However, the global index alone is insufficient, as sibling vertices that share the same parent with close indices may require distinct posterior dynamics driven by the different observations in their respective subtrees, or the vertices sharing close indices may have distinct parents. To resolve this ambiguity, we condition the shared network on additional edge-specific context.

**Discrete dynamics** We parameterize the discrete transition map using a shared neural network  $F_v^\theta(\tilde{x}') = F^\theta(\tilde{x}', x_{\text{pa}(v)}, c_v)$ . Conditioning on the parent state  $x_{\text{pa}(v)}$  is essential, as it allows the flow to apply state-dependent non-linear corrections where the linear proposal deviates from the true posterior. The context identifier  $c_v$  further enables the model to adapt to branch-specific heterogeneity across the topology.

**Continuous dynamics** Similarly, for continuous edges, we define the residual drift using a shared parameterization

$s_v^\theta(t, z) = s^\theta(t, z, \tilde{\mu}_v, T_v, c_v)$ . We condition on the child's guided proposal mean  $\tilde{\mu}_v$  to inject specific "look-ahead" guidance from the subtree's observations. Furthermore, explicitly including the edge duration  $T_v$  resolves temporal ambiguities (e.g., distinguishing fast vs. slow transitions), allowing the network to scale the drift magnitude according to the specific time horizon.

## 5. Experiments

We validate our method through a series of experiments. First, we benchmark it in two linear models where the exact smoothing distributions can be computed in closed form, which are used to assess scalability across varying tree sizes and dimensions in regular and irregular trees. Second, we stress-test the method on a synthetic multimodal non-linear system. Specifically, we demonstrate that while the guided proposal and the MCMC correction suffer from mode collapse, our method robustly recovers the full posterior landscape. Finally, we deploy the method on a high-dimensional phylogenetic inference task, reconstructing ancestral butterfly wing morphologies from real-world data.

### 5.1. Linear Gaussian model

To validate our method, we consider  $d$ -dimensional linear Gaussian transitions on a balanced tree with depth  $N_{\text{depth}}$  and each vertex branching into  $N_{\text{branch}}$  children. The discrete edge transitions follow  $P(x, dx') = \varphi(x'; \sqrt{1 - \alpha}x, \alpha\mathbf{I})dx'$ , with leaf observations  $Y_l \sim \mathcal{N}(X_l, \Sigma_{\text{obs}})$ . We also assume a fixed root  $X_0 = x_0$ ; no pseudo root is needed. This model is invariant for the  $\mathcal{N}(0, \mathbf{I})$ -distribution for any  $\alpha \in (0, 1)$ . This setup admits exact computation of the posterior, the Rauch-Tung-Striebel (RTS) smoother, providing a lower bound for the loss:  $\mathcal{J}^* = -\log h_0(x_0)$ . To assess the model's ability to learn drift corrections, we intentionally misspecify the auxiliary process as a zero-drift random walk:  $\tilde{P}(x, dx') = \varphi(x'; x, \alpha\mathbf{I})dx'$ . We evaluate scalability across tree sizes ( $N_{\text{depth}}$  and  $N_{\text{branch}}$ ) and state dimensions  $d$ , reporting relative errors  $(\bar{\mathcal{J}} - \mathcal{J}^*)/\mathcal{J}^*$  in Figure 1, where  $\bar{\mathcal{J}}$  denotes the average loss over the final 500 training steps. Further details can be found in Section B.2.

Notably, the approximation error decreases as the tree topology expands. This trend is attributed to the data efficiency of amortized inference; the global sharing of the network parameters across larger trees yields denser gradient signals that facilitate optimization and refine the posterior approximation. Conversely, increasing the state dimension leads to a rise in error, reflecting the inherent challenges of the curse of dimensionality and numerical errors. Despite this increase, the error remains on the order of  $10^{-2}$ , demonstrating the method's capacity to exploit structural redundancy for large-scale inference while maintaining robustness in high-dimensional state spaces.

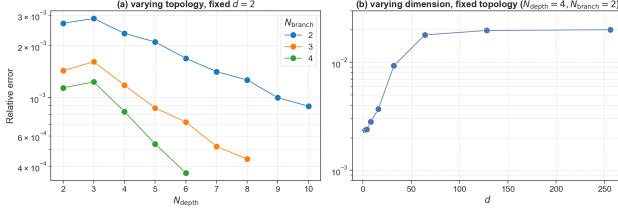


Figure 1. Validation on Linear Gaussian Benchmarks. We compare the converged training loss against the analytical RTS smoother baseline. (a) Topological Scalability: Relative error decreases as tree complexity ( $N_{\text{depth}}$ ,  $N_{\text{branch}}$ ) grows, showing that our path-wise amortization effectively leverages larger datasets rather than degrading. (b) Dimensional Scalability: The method remains robust in high dimensions, with relative error bounded below 3% even as state space grows to  $d = 256$ .

## 5.2. Ornstein-Uhlenbeck model

We then consider an Ornstein-Uhlenbeck (OU) model, which is frequently employed in tree-structured probabilistic frameworks to model continuous trait evolution in phylogenetic analysis (e.g., (Marguerite et al., 2004)). The continuous transition along an edge  $(\text{pa}(v), v)$  with length of  $T_v$  is governed by SDE:  $dZ_v(t) = \alpha(\Theta - Z_v(t))dt + \sigma dW_t$ , where  $\alpha \in \mathbb{R}^{d \times d}$  is a matrix with eigenvalues having strictly positive real parts,  $\Theta \in \mathbb{R}^d$  represents the long-term mean, and  $\sigma \in \mathbb{S}_+^d$  denotes the diffusion coefficient. Values used in our simulation results for  $(\alpha, \Theta, \sigma)$  are specified in Section B.3. We examine the case where  $d = 2$ , and leaf observations are sampled as  $Y_l \sim \mathcal{N}(Z_v(T_l), \Sigma_{\text{obs}})$ , i.e., we only observed at the final state of evolution. We also construct a synthetic random tree topology to evaluate the robustness of our method in an irregular tree, whose topology is illustrated in Figure 6. For the auxiliary process, we adopt a standard Brownian motion by selecting  $B = \beta = 0$  and  $\tilde{\sigma} = \sigma$ . Due to the drift mismatch, relying solely on the proxy guidance  $\nabla \log \tilde{h}$  results in posterior deviation. We investigate whether the amortized neural network  $s_\theta$  can effectively bridge this gap.

We consider three representative positions within the tree: (a) a shallow vertex close to the root, where observational information has been attenuated over long distances and subjected to high variance due to aggregation at multiple branching points; (b) a medium vertex situated on the mid of a direct lineage, where the information flow remains relatively distinct due to fewer branching events; and (c) a deep leaf, where the posterior is most heavily influenced by local observations. We compare the empirical distributions of the learned variational posterior and the auxiliary proposal process against the analytical ground truth obtained via the RTS smoother, and present the empirical distributions of these positions in Figure 2.

As shown in the figure, the uncorrected guided proposal exhibits a visible spatial bias relative to the RTS ground truth. In contrast, the learned variational samples consis-

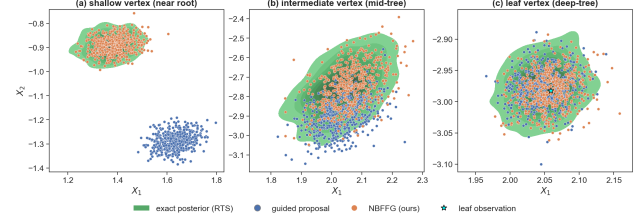


Figure 2. Empirical distributions of 500 independent samples of the guided proposal (gray) and the learned variational posterior (orange) against the analytical ground truth (RTS, green contours) at different tree depths.

tently align with the true posterior contours across all depths. The amortized network successfully compensates for inherited drift errors at shallow vertices and accurately concentrates the distribution around high-precision observations at deep leaves. These results confirm that the learned score correction recovers both the mean and the analytical covariance structure. Additional experimental details are provided in Section B.3.

## 5.3. Double-well diffusion

To validate performance under non-linear dynamics, we simulate a double-well SDE,  $dZ_v(t) = -\nabla[\alpha(Z_v(t)^2 - 1)^2]dt + \sigma dW_t$ , on a three-layer binary tree rooted at a fixed point  $x_0 = 0$ . We assign long durations ( $T = 4.0$ ) to root-connected edges and short durations ( $T = 1.0$ ) to leaf edges. The parameters  $\alpha$  and  $\sigma$  are chosen such that trajectories rapidly collapse to the stable modes at  $\pm 1$ , resulting in a multimodal prior over the leaves with four equiprobable configurations. Specifically,  $[1, 1, 1, 1]^\top$ ,  $[1, 1, -1, -1]^\top$ ,  $[-1, -1, 1, 1]^\top$ , and  $[-1, -1, -1, -1]^\top$ . We condition the leaves on the specific "mixed" observation  $y = [-1, -1, 1, 1]^\top$  with  $Y_l \sim \mathcal{N}(X_l, \Sigma_{\text{obs}})$ . This creates a challenging inference scenario: while the forward prior is multimodal, the posterior is unimodal. To succeed, the model must infer that the top branch commits to  $+1$  and the bottom branch to  $-1$  shortly after the root. This tests the method's ability to provide correct directional guidance early in the topology, rather than merely fitting observations locally at the leaves.

Figure 9 compares the path distributions generated by: (a) the unconditioned prior; (b) the guided proposal (using  $B = \beta = 0, \tilde{\sigma} = \sigma$ ); (c) the guided proposal corrected by MCMC where the driving Wiener increments are updated by the preconditioned Crank-Nicolson scheme (serving as the ground truth reference) (van der Meulen & Sommer, 2026); and (d) our learned variational posterior. As shown in (b), the guidance proposal fails to enforce early lineage separation; the trajectories remain entangled near the root and are forced to cross rapidly in the final stages to satisfy leaf constraints. This failure stems from the dissipation of the linear guiding signal over the long time horizon, which leaves the process unguided near the root, where early commitment is critical. In contrast, the variational posterior (d)—closely

matching the MCMC reference (c)—successfully identifies the bifurcation immediately. The trajectories separate early toward the four distinct leaf targets (clustered around  $\pm 1$ ) without overlapping. This demonstrates that the learned neural residual effectively amplifies the asymmetric evidence from the leaves, propagating it back to the root to resolve mode ambiguity. Furthermore, we also evaluate another setup that yields a bimodal posterior. In this case, the MCMC often struggles with covering both modes, while our method successfully recovers the bimodality (see Section B.4 for details).

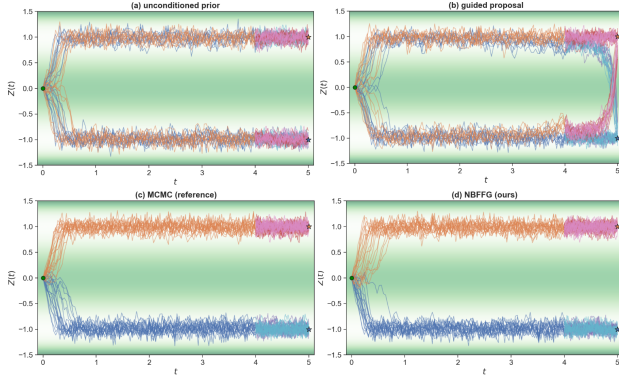


**Figure 3.** Visualization of double-well diffusion conditioned on the leaf observation  $[-1, -1, 1, 1]^\top$  on a binary tree. The figure displays 20 samples from (a) the prior; (b) the raw guided proposal; (c) the corrected guided proposal with MCMC; (d) the learned variational posterior. Trajectories belonging to the same edge are identified by color. For example, in (a), the orange paths (leading to one of the children of the root) show that the process moves with equal probability to either of the modes at  $+1$  and  $-1$ . In the transition from time 4.0 to 5.0, the process remains in the same mode. Green dots at  $t = 0.0$  represent the root, and stars at  $t = 5.0$  represent the observed values  $\pm 1$  at the leaf nodes. The background green shading illustrates the potential wells.

#### 5.4. Stochastic phylogenetic shape evolution

Finally, we consider a high-dimensional application: modeling the stochastic morphological evolution of butterfly wings. In evolutionary biology, species morphology can be treated as a set of phenotypic traits that evolve stochastically along a phylogenetic tree. While linear models, such as Brownian motion or Ornstein-Uhlenbeck processes, are standard in phylogenetic analysis (e.g., (Felsenstein, 1981; Marguerite et al., 2004)), a nonlinear framework is required to preserve the topological integrity of the shapes throughout the evolutionary process. To address this, we employ the Kunita flow, a process whose theoretical foundations are established in (Sommer et al., 2025) and which has demonstrated efficacy in biological data applications (Stroustrup et al., 2025). Given observations of morphology at the current time, i.e., at the leaves of the phylogenetic tree, we aim to estimate the evolutionary process at prior times, especially at the internal vertices that lack observed evidence.

We consider the family of *Papilio* butterflies, whose phy-

logenetic tree topology is illustrated in the top panel of Figure 4. Our objective is to perform ancestral reconstruction—inferring the unobserved posterior distributions of all internal vertices, particularly the root, conditioned solely on the high-dimensional shape contours of extant species at the leaves. The bottom panel visualizes the learned posterior means for selected ancestors alongside their relevant observations. Notably, the reconstructed root (Species 1) captures a plausible morphology derived from the diverse leaf population, while intermediate vertices (e.g., Species 20 and 26) exhibit shapes that bridge their specific descendants (e.g., *P. ambrax* vs. *P. antimachus*). These results establish NBFFG as a framework for continuous-trait phylogenetic inference, capable of recovering evolutionary histories directly from complex, high-dimensional observational data. (See Figure 11 and Section B.5 for the complete atlas of reconstructed shapes and configuration details).

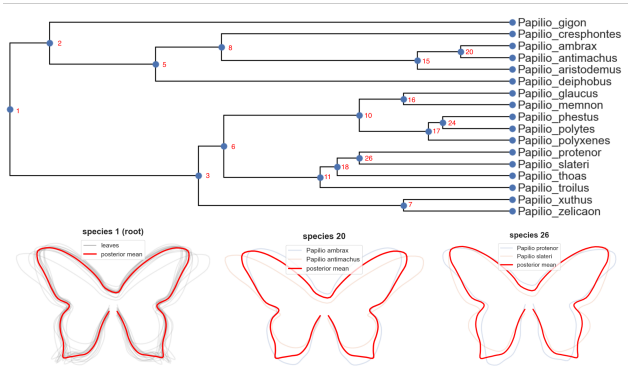


**Figure 4.** Phylogenetic tree topology and ancestral shape reconstruction. (top) The *Papilio* family tree topology, where nodes (blue dots) represent ancestral lineages and tips represent extant species. (bottom) Reconstructed posterior mean shape of the ancestors (red) overlaid with the observed morphological variation of their leaf species (gray or colored shade curves).

## 6. Conclusions

We propose Neural Backward Filtering Forward Guiding (NBFFG), a unified framework for Bayesian smoothing on a directed tree that generalizes across both discrete-time transitions and continuous-time diffusions. By combining analytical approximations with learnable neural corrections, NBFFG offers a computationally efficient alternative to traditional MCMC and SMC pipelines while maintaining high inference fidelity. Extensive experiments—ranging from irregular topologies to high-dimensional biological data—validate the method’s correctness and scalability. However, a remaining constraint is the reliance on back-propagating through the entire temporal path, even with importance sampling. Future research will address this by developing simulation-free training schemes, potentially leveraging the self-consistency properties of Doob’s  $h$ -function (Howard et al., 2025).

## Impact Statement

This paper presents work whose goal is to advance the field of Machine Learning and Statistics. There are many potential societal consequences of our work, none of which we feel must be specifically highlighted here.

## References

Baker, E. L., Schauer, M., and Sommer, S. Score matching for bridges without learning time-reversals, 2025.

Bardel, N. and Desbouvries, F. Exact Bayesian Prediction in a Class of Markov-switching Models. *Methodology and Computing in Applied Probability*, 14(1): 125–134, 2012. ISSN 1387-5841, 1573-7713. doi: 10.1007/s11009-010-9189-4.

Bovier, A. *Gaussian processes on trees: From spin glasses to branching Brownian motion*, volume 163. Cambridge University Press, 2017.

Briers, M., Doucet, A., and Maskell, S. Smoothing algorithms for state-space models. *Annals of the Institute of Statistical Mathematics*, 62(1):61–89, 2010. ISSN 0020-3157, 1572-9052. doi: 10.1007/s10463-009-0236-2.

Carter, C. K. and Kohn, R. On Gibbs sampling for state space models. *Biometrika*, 81(3):541–553, 1994.

Chen, R. T., Rubanova, Y., Bettencourt, J., and Duvenaud, D. K. Neural ordinary differential equations. In *Advances in neural information processing systems*, volume 31, 2018.

Chopin, N., Fulop, A., Heng, J., and Thiery, A. H. Computational Doob h-transforms for Online Filtering of Discretely Observed Diffusions. In *Proceedings of the 40th International Conference on Machine Learning*, pp. 5904–5923. PMLR, 2023.

Chou, K., Willsky, A., and Benveniste, A. Multiscale recursive estimation, data fusion, and regularization. *IEEE Transactions on Automatic Control*, 39(3):464–478, 1994. ISSN 00189286. doi: 10.1109/9.280746.

Delyon, B. and Hu, Y. Simulation of conditioned diffusions, 2006.

Desbouvries, F., Lecomte, J., and Pieczynski, W. Kalman filtering in pairwise Markov trees. *Signal Processing*, 86 (5):1049–1054, 2006. ISSN 01651684. doi: 10.1016/j.sigpro.2005.07.026.

Felsenstein, J. Evolutionary trees from DNA sequences: A maximum likelihood approach. *Journal of Molecular Evolution*, 17(6):368–376, 1981. ISSN 1432-1432. doi: 10.1007/BF01734359.

Frühwirth-Schnatter, S. Data augmentation and dynamic linear models. *Journal of time series analysis*, 15(2): 183–202, 1994.

Guarniero, P., Johansen, A. M., and Lee, A. The Iterated Auxiliary Particle Filter. *Journal of the American Statistical Association*, 112(520):1636–1647, 2017. ISSN 0162-1459, 1537-274X. doi: 10.1080/01621459.2016.1222291.

Heng, J., Bishop, A. N., Deligiannidis, G., and Doucet, A. Controlled sequential Monte Carlo. *The Annals of Statistics*, 48(5), 2020. ISSN 0090-5364. doi: 10.1214/19-AOS1914.

Heng, J., De Bortoli, V., Doucet, A., and Thornton, J. Simulating diffusion bridges with score matching. *Biometrika*, 112(4):asaf048, 2025. ISSN 1464-3510. doi: 10.1093/biomet/asaf048.

Howard, S., Nüsken, N., and Pidstrigach, J. Control Consistency Losses for Diffusion Bridges. In *The Thirty-ninth Conference on Neural Information Processing Systems (NeurIPS 2025) Workshop: Frontiers in Probabilistic Inference: Sampling Meets Learning.*, 2025. doi: 10.48550/arXiv.2512.05070.

Huelsenbeck, J. P., Nielsen, R., and Bollback, J. P. Stochastic mapping of morphological characters. *Systematic biology*, 52(2):131–158, 2003.

Kempe, D., Kleinberg, J., and Tardos, É. Maximizing the spread of influence through a social network. In *Proceedings of the ninth ACM SIGKDD international conference on Knowledge discovery and data mining*, pp. 137–146, 2003.

Lawson, D., Raventós, A., Warrington, A., and Linderman, S. SI $\chi$ O: Smoothing Inference with Twisted Objectives. In *Proceedings of the 36th International Conference on Neural Information Processing Systems*, volume 35, pp. 38844–38858, 2022.

Lawson, D., Li, M. Y., and Linderman, S. W. NAS- $\chi$ : Neural Adaptive Smoothing via Twisting. In *Proceedings of the 37th International Conference on Neural Information Processing Systems*, pp. 8602–8633, 2023.

Marguerite, A. B., Aaron, A. K., Price, A. E. T., and Crespi, B. J. Phylogenetic comparative analysis: A modeling approach for adaptive evolution. *The American Naturalist*, 164(6):683–695, 2004. ISSN 00030147, 15375323.

Mider, M., Schauer, M., and van der Meulen, F. Continuous-discrete smoothing of diffusions. *Electronic Journal of Statistics*, 15(2), 2021. ISSN 1935-7524. doi: 10.1214/21-EJS1894.

Paige, B. and Wood, F. Inference networks for sequential Monte Carlo in graphical models. In *International Conference on Machine Learning*, pp. 3040–3049. PMLR, 2016.

Pearl, J. *Probabilistic Reasoning in Intelligent Systems: Networks of Plausible Inference*. Morgan Kaufmann, 1988.

Rauch, H. E., Tung, F., and Striebel, C. T. Maximum likelihood estimates of linear dynamic systems. *AIAA Journal*, 3(8):1445–1450, 1965. doi: 10.2514/3.3166. URL <https://doi.org/10.2514/3.3166>.

Sarkka, S. *Bayesian Filtering and Smoothing*, volume 2023. Cambridge University Press, 2023.

Schauer, M., van der Meulen, F., and van Zanten, H. Guided proposals for simulating multi-dimensional diffusion bridges. *Bernoulli*, 23(4A), 2017. ISSN 1350-7265. doi: 10.3150/16-BEJ833.

Sommer, S., Yang, G., and Baker, E. L. Stochastics of shapes and kunita flows, 2025. URL <https://arxiv.org/abs/2512.11676>.

Stroustrup, S., Pedersen, M. A., van der Meulen, F., Sommer, S., and Nielsen, R. Stochastic phylogenetic models of shape. *bioRxiv*, 2025. doi: 10.1101/2025.04.03.646616. URL <https://www.biorxiv.org/content/early/2025/04/08/2025.04.03.646616>.

van der Meulen, F. and Sommer, S. Backward filtering forward guiding. *Journal of Machine Learning Research*, 2026.

Yang, G. Neural Guided Diffusion Bridges. In *Forty-Second International Conference on Machine Learning*. PMLR, 2025.

## A. Theoretical details

### A.1. Details on the guided proposals

We review some of the main results from (van der Meulen & Sommer, 2026)[Theorem 14, 23] on the computation of guided proposals.

Suppose the edge  $(\text{pa}(v), v)$  is discrete and modelled by the transition kernel:

$$\mathbb{P}_v(X_v \in dx' \mid X_{\text{pa}(v)} = x) = P_v(x, dx') = \varphi(x'; Bx + \beta, \tilde{\Sigma}). \quad (25)$$

For each  $v \in \mathcal{V}$  (including the root), the score of the  $h$ -function is given by

$$\nabla \log h_v(x) = - \sum_{c \in \text{ch}(v)} H_{v,c} x + \sum_{c \in \text{ch}(v)} \eta_{v,c}, \quad (26)$$

where  $H_{v,c}, \eta_{v,c}$  are defined as

$$H_{v,c} := B^\top (H_c^{-1} + \tilde{\Sigma})^{-1} B^\top, \quad \eta_{v,c} := B^\top (H_c^{-1} + \tilde{\Sigma})^{-1} (H_c^{-1} \eta_c - \beta). \quad (27)$$

Here  $H_c, \eta_c$  are the precision and potential at child  $c$ , which are computed from their children by applying Equation (26) recursively.

For a general nonlinear Gaussian transition as defined in Equation (2), the guided proposal defined by Equation (4) with Equation (26) is Gaussian  $\mathcal{N}(\tilde{\mu}(x), \tilde{\Sigma}(x))$  with mean and covariance

$$\tilde{\mu}(x) = \tilde{\Sigma}(x)(\eta_v + \Sigma(x)^{-1} \mu(x)), \quad \tilde{\Sigma}(x) = (H_v + \Sigma(x)^{-1})^{-1}. \quad (28)$$

For a continuous edge  $(\text{pa}(v), v)$  where the transition is governed by the SDE

$$dZ_v(t) = [B(t)Z_v(t) + \beta(t)]dt + \tilde{\sigma}(t)dW_t. \quad (29)$$

We have that for each  $v \in \mathcal{V}$  and its child  $c \in \text{ch}(v)$ , the score of the  $h$ -function of the state  $(t, z) \in (0, T_c] \times \mathbb{R}^d$  is given by

$$\nabla \log h_v(t, z) = -H(t)z + \eta(t), \quad (30)$$

where on  $t \in (0, T_v]$ ,  $(H(t), \eta(t))$  solve the ODEs

$$dH(t) = -[B(t)^\top H(t) + H(t)B(t) - H(t)\tilde{\Sigma}(t)H(t)]dt, \quad (31a)$$

$$d\eta(t) = -[B(t)^\top \eta(t) + H(t)\tilde{\Sigma}(t)\eta(t) - H(t)\beta(t)]dt, \quad (31b)$$

subject to  $H(T_c) = H_c, \eta(T_c) = \eta_c$ , and  $\tilde{\Sigma}(t) := \tilde{\sigma}(t)\tilde{\sigma}(t)^\top$ . At  $t = 0$ ,

$$\nabla \log h_v(0, z) = - \sum_{c \in \text{ch}(v)} H(0^+)z + \sum_{c \in \text{ch}(v)} \eta(0^+), \quad (32)$$

where  $H(0^+), \eta(0^+)$  are the solutions of Equation (31) at time  $0^+$ . The guided proposal's dynamics are governed by the SDE

$$dZ_v(t) = [b(Z_v(t)) + \Sigma(Z_v(t))\nabla \log h_v(t, Z_v(t))]dt + \sigma(Z_v(t))dW_t^{\tilde{\Pi}_v}. \quad (33)$$

At the leaves, assume the observation model is Gaussian, which takes the form of  $\mathbb{L}(Y \mid X) = \mathcal{N}(X, \Sigma_{\text{obs}})$  with the observation noise covariance  $\Sigma_{\text{obs}}$ , then  $H, \eta$  are initialized at leaf  $l \in \mathcal{L}$  as  $H_l = \Sigma_{\text{obs}}^{-1}$  and  $\eta_l = H_l y_l$ , where  $y_l$  is the observed realization of leaf  $X_l$ .

## A.2. Proof of Theorem 4.1

*Proof.* We start with the definition of KL divergence:

$$D_{\text{KL}}(\mathbb{Q}^\theta \parallel \Pi) = \mathbb{E}_{\mathbb{Q}^\theta} \left[ \log \frac{d\mathbb{Q}^\theta}{d\Pi}(X_{\mathcal{V}^+}) \right] = \mathbb{E}_{\mathbb{Q}^\theta} \left[ \log \frac{d\mathbb{Q}^\theta}{d\Pi}(X_{\mathcal{V}^+}) - \log \frac{d\Pi}{d\Pi}(X_{\mathcal{V}^+}) \right]. \quad (34)$$

By definitions of  $\mathbb{Q}^\theta$ ,  $\mathbb{P}$  and  $\Pi$ ,

$$\mathbb{E}_{\mathbb{Q}^\theta} \left[ \log \frac{d\mathbb{Q}^\theta}{d\Pi}(X_{\mathcal{V}^+}) - \log \frac{d\Pi}{d\Pi}(X_{\mathcal{V}^+}) \right] = \mathbb{E}_{\mathbb{Q}^\theta} \left[ \sum_{v \in \mathcal{V}^+} \log \frac{d\mathbb{Q}_v^\theta}{d\Pi_v}(X_v) - \sum_{v \in \mathcal{V}^+} \log \frac{d\Pi_v}{d\Pi_v}(X_v) \right] \quad (35)$$

The first term reduces to  $\sum_{v \in \mathcal{V}^+} D_{\text{KL}}(\mathbb{Q}_v^\theta \parallel \mathbb{P}_v)$ . For the second term, we now establish that the Radon-Nikodym derivative takes a consistent form regardless of the edge dynamics:

- For a discrete edge  $(\text{pa}(v), v)$ , the posterior transition density is given directly by Equation (4):

$$\frac{d\Pi_v}{d\Pi_v}(X_v) = \frac{\Pi_v(X_{\text{pa}(v)}, dX_v)}{P_v(X_{\text{pa}(v)}, dX_v)} = \frac{h_v(X_v)}{h_{\text{pa}(v),v}(X_{\text{pa}(v)})}, \quad (36)$$

where the denominator is defined as the integral  $h_{\text{pa}(v),v}(x) = \int h_v(x') P^v(x, dx')$ .

- For a continuous edge defined over  $t \in [0, T_v]$ , the posterior path measure satisfies Equation (5). Evaluating this change of measure at the terminal time  $t = T_v$  yields:

$$\frac{d\Pi_v}{d\Pi_v} = \frac{h_v(T_v, Z_v(T_v))}{h_v(0, Z_v(0))}. \quad (37)$$

Identifying the process endpoints with the vertex states— $Z_v(0) = X_{\text{pa}(v)}$  and  $Z_v(T_v) = X_v$ —we can unify the notation with the discrete case. First, we identify the vertex-level function  $h_v(\cdot)$  with the terminal value of the continuous  $h$ -function, i.e.,  $h_v(x) \equiv h_v(T_v, x)$ . Second, we observe that the denominator  $h_v(0, Z_v(0))$  represents the expected future likelihood given the initial state. We unify this with the discrete notation by defining:

$$h_{\text{pa}(v),v}(x) := h_v(0, x) = \mathbb{E}_{\mathbb{P}_v} [h_v(X_v) \mid X_{\text{pa}(v)} = x]. \quad (38)$$

Note that while the discrete case computes this expectation via direct integration (Equation (9)), the continuous case computes it by solving the Kolmogorov backward equation (Equation (10)) at  $t = 0$ .

Substituting these definitions back into the continuous derivative, we obtain the unified expression for both edge types. We then follow the derivation in (van der Meulen & Sommer, 2026):

$$\sum_{v \in \mathcal{V}^+} \log \frac{d\Pi_v}{d\Pi_v}(X_v) = \log \prod_{v \in \mathcal{V}^+} \frac{h_v(X_v)}{h_{\text{pa}(v),v}(X_{\text{pa}(v)})} \quad (39a)$$

$$= \log \frac{\prod_{v \in \mathcal{V}^+} \prod_{c \in \text{ch}(v)} h_{v,c}(X_v)}{\prod_{v \in \mathcal{V}^+} h_{\text{pa}(v),v}(X_{\text{pa}(v)})} \quad (39b)$$

$$= \log \frac{\left( \prod_{v \in \mathcal{V}^+ \setminus \mathcal{L}} \prod_{c \in \text{ch}(v)} \overbrace{h_{v,c}(X_v)} \right) \left( \prod_{l \in \mathcal{L}} \prod_{c \in \text{ch}(l)} h_{l,c}(X_l) \right)}{\left( \prod_{c \in \text{ch}(\mathbf{0})} h_{\mathbf{0},c}(X_{\mathbf{0}}) \right) \left( \prod_{v \in \mathcal{V}^+ \setminus \mathcal{L}} \prod_{c \in \text{ch}(v)} \overbrace{h_{v,c}(X_v)} \right)} \quad (39c)$$

$$= \log \frac{\prod_{k \in \mathcal{L}} \prod_{c \in \text{ch}(k)} h_{k,c}(X_k)}{h_{\mathbf{0}}(x_{\mathbf{0}})}. \quad (39d)$$

Note that the second equality comes from the definition of  $h_v$  by fusion Equation (8). The third equivalence follows by regrouping  $\mathcal{V}^+$  as non-leaf vertices  $\mathcal{V}^+ \setminus \mathcal{L}$  and leaves  $\mathcal{L}$ . Since the leaf vertices have no children,  $\prod_{c \in \text{ch}(l)} h_{l,c}(X_l) = h_l(X_l) = \ell(y_l \mid X_l)$ . Therefore,

$$\sum_{v \in \mathcal{V}^+} \log \frac{d\Pi_v}{d\Pi_v}(X_v) = \sum_{l \in \mathcal{L}} \log \ell(y_l \mid X_l) - \log h_{\mathbf{0}}(x_{\mathbf{0}}). \quad (40)$$

Combining both terms, we obtain:

$$D_{\text{KL}}(\mathbb{Q}^\theta \parallel \Pi) = \underbrace{\sum_{v \in \mathcal{V}^+} D_{\text{KL}}(\mathbb{Q}_v^\theta \parallel \mathbb{P}_v) - \sum_{l \in \mathcal{L}} \log \ell(y_l \mid X_l)}_{\mathcal{J}(\theta)} + \log h_{\mathbf{0}}(x_{\mathbf{0}}). \quad (41)$$

□

### A.3. Proof of Corollary 4.2

*Proof.* We only need to compute the edge-specific KL divergence  $D_{\text{KL}}(\mathbb{Q}_v^\theta \parallel \mathbb{P}_v)$ . By definition:

$$D_{\text{KL}}(\mathbb{Q}_v^\theta \parallel \mathbb{P}_v) = \mathbb{E}_{\mathbb{Q}_v^\theta} \left[ \log \frac{d\mathbb{Q}_v^\theta}{d\mathbb{P}_v}(X_v) \right] = \mathbb{E}_{q_v^\theta} \left[ \log \frac{q_v^\theta(X_v \mid X_{\text{pa}(v)})}{p_v(X_v \mid X_{\text{pa}(v)})} \right]. \quad (42)$$

By construction:

$$\log q_v^\theta(x' \mid x) = \log \tilde{\pi}_v(\tilde{x}' \mid x) - \log |\det J_{F_v^\theta}(\tilde{x}')|. \quad (43)$$

Substitute it into the  $D_{\text{KL}}(\mathbb{Q}_v^\theta \parallel \mathbb{P}_v)$  and we obtain the stated result. □

### A.4. Proof of Corollary 4.3

*Proof.* To compute the edge-wise KL divergence  $D_{\text{KL}}(\mathbb{Q}_v^\theta \parallel \mathbb{P}_v)$ , recall:

$$\frac{d\mathbb{Q}_v^\theta}{d\mathbb{P}_v}(Z_v) = M_v(T_v) := \exp \left( \int_0^{T_v} g_v^\theta(t, Z_v(t))^\top \sigma(Z_v(t)) dW_t^\mathbb{P} - \frac{1}{2} \int_0^{T_v} \|g_v^\theta(t, Z_v(t))\|_{\Sigma(Z_v(t))}^2 dt \right). \quad (44)$$

By Girsanov's theorem,  $W_t^{\mathbb{Q}_v^\theta} := W_t^\mathbb{P} - \int_0^t \sigma(Z_v(s))^\top g_v^\theta(s, Z_v(s)) ds$  is a  $\mathbb{Q}_v^\theta$ -Wiener process. Therefore, by the definition of KL divergence,

$$D_{\text{KL}}(\mathbb{Q}_v^\theta \parallel \mathbb{P}_v) = \mathbb{E}_{\mathbb{Q}_v^\theta} \left[ \log \left( \frac{d\mathbb{Q}_v^\theta}{d\mathbb{P}_v}(Z_v) \right) \right] \quad (45a)$$

$$= \mathbb{E}_{\mathbb{Q}_v^\theta} \left[ \int_0^{T_v} g_v^\theta(t, Z_v(t))^\top \sigma(Z_v(t)) dW_t^{\mathbb{P}_v} - \frac{1}{2} \int_0^{T_v} \|g_v^\theta(t, Z_v(t))\|_{\Sigma(Z_v(t))}^2 dt \right] \quad (45b)$$

$$= \mathbb{E}_{\mathbb{Q}_v^\theta} \left[ \int_0^{T_v} g_v^\theta(t, Z_v(t))^\top \sigma(Z_v(t)) dW_t^{\mathbb{Q}_v^\theta} + \frac{1}{2} \int_0^{T_v} \|g_v^\theta(t, Z_v(t))\|_{\Sigma(Z_v(t))}^2 dt \right] \quad (45c)$$

$$= \mathbb{E}_{\mathbb{Q}_v^\theta} \left[ \frac{1}{2} \int_0^{T_v} \|g_v^\theta(t, Z_v(t))\|_{\Sigma(Z_v(t))}^2 dt \right]. \quad (45d)$$

The first Itô integral vanishes because of the zero-mean property. □

### A.5. Proof of Proposition 4.4

*Proof.* To show this, we write:

$$\mathbb{E}_{l \sim \gamma} [\mathcal{J}'(\theta; l)] = \mathbb{E}_{l \sim \gamma} \left[ \sum_{v \in \mathcal{V}_l^+} \frac{D_{\text{KL}}(\mathbb{Q}_v^\theta \parallel \mathbb{P}^v)}{\omega(v)} - \frac{\log \ell(y_l \mid X_l)}{\gamma(l)} \right] \quad (46a)$$

$$= \mathbb{E}_{l \sim \gamma} \left[ \sum_{v \in \mathcal{V}_l^+} \frac{D_{\text{KL}}(\mathbb{Q}_v^\theta \parallel \mathbb{P}^v)}{\omega(v)} \right] - \mathbb{E}_{l \sim \gamma} \left[ \frac{1}{\gamma(l)} \log \ell(y_l \mid X_l) \right] \quad (46b)$$

$$= \sum_{k \in \mathcal{L}} \gamma(k) \left( \sum_{v \in \mathcal{V}_k^+} \frac{D_{\text{KL}}(\mathbb{Q}_v^\theta \parallel \mathbb{P}^v)}{\omega(v)} \right) - \sum_{k \in \mathcal{L}} \gamma(k) \left( \frac{1}{\gamma(k)} \log \ell(y_k \mid X_k) \right) \quad (46c)$$

$$= \sum_{k \in \mathcal{L}} \gamma(k) \left( \sum_{v \in \mathcal{V}^+} \frac{D_{\text{KL}}(\mathbb{Q}_\theta^v \parallel \mathbb{P}^v)}{\omega(v)} \mathbb{1}(v \in \mathcal{V}_k^+) \right) - \sum_{k \in \mathcal{L}} \log \ell(y_k \mid X_k) \quad (46d)$$

$$= \sum_{v \in \mathcal{V}^+} \frac{D_{\text{KL}}(\mathbb{Q}_\theta^v \parallel \mathbb{P}^v)}{\omega(v)} \underbrace{\sum_{k \in \mathcal{L}} \gamma(k) \mathbb{1}(v \in \mathcal{V}_k^+)}_{\omega(v)} - \sum_{k \in \mathcal{L}} \log \ell(y_k \mid X_k) \quad (46e)$$

$$= \sum_{v \in \mathcal{V}^+} D_{\text{KL}}(\mathbb{Q}_\theta^v \parallel \mathbb{P}^v) - \sum_{k \in \mathcal{L}} \log \ell(y_k \mid X_k). \quad (46f)$$

We then finish the proof.  $\square$

## B. Experiment details

### B.1. Implementation details

**Backward information filter** Deriving  $\tilde{h}$  requires solving either Equation (9) or Equation (10). One crucial numerical instability lies in the case where  $\sigma_{\text{obs}} \rightarrow 0$ , leading the leaf initialization  $H_l = \Sigma_{\text{obs}}^{-1}$  to explode. To address this, for the discrete case, let  $\tilde{P}_v \equiv \tilde{\Sigma}_v^{-1}$ , we applied the Woodbury identities:  $Q_{v,c}^{-1} = (\tilde{\Sigma}_v + H_c^{-1})^{-1} = \tilde{P}_v - \tilde{P}_v(\tilde{P}_v + H_c)\tilde{P}_v$ , and  $Q_{v,c}^{-1}H_c^{-1} = (\tilde{\Sigma}_v + H_c^{-1})^{-1}H_c^{-1} = \tilde{P}_v(\tilde{P}_v + H_c)^{-1}$  to avoid inverting  $H_c$  directly. For the continuous case, we applied an explicit 5th-order Runge-Kutta solver with fixed step size on a predefined discrete time grid  $\{t_i\}$ , and the solutions  $H(t_i)$ ,  $\eta(t_i)$  are stored. While forward simulating the variational SDE, the same time grid is deployed with the precomputed  $H$  and  $\eta$ .

**Topology embedding** As discussed, both  $F^\theta$  and  $s^\theta$  is conditioned on the global vertex index embedding  $c_v \in \mathbb{R}^{d_n}$ , where  $d_n$  is the embedding dimension. We pick  $d_n = 16$  if the tree size is below 100 or  $d_n = 64$  if the tree size is between 100 and 10,000. Larger trees with a size over 10,000 require other techniques of conditioning on the topology, which deserves further research.

**Normalizing flow** The mapping  $F^\theta$ , is constructed by composing a sequence of bijections,  $f^\theta : x \mapsto y$ , implemented as affine coupling layers within a RealNVP framework. For each bijection, the transformation is defined as:

$$y_{1:d//2} = x_{1:d//2}, \quad y_{d//2+1:d} = x_{d//2+1:d} \odot \exp(\text{scale}^\theta(x_{1:d//2}, c)) + \text{trans}^\theta(x_{1:d//2}, c), \quad (47)$$

where  $\text{scale}^\theta$ ,  $\text{trans}^\theta$  are two MLPs, and  $c = [c_v, x_{\text{pa}(v)}]$  represents the conditional context. The Jacobian determinant of this transformation is efficiently computed as:  $\det(J_{f^\theta}) = \exp\left(\sum_{i=1}^{d-d//2} \text{scale}^\theta(x_{1:d//2}, c)_i\right)$ . Specifically, in the univariate case ( $d = 1$ ), the inputs to  $\text{scale}^\theta$  and  $\text{trans}^\theta$  depend exclusively on  $c$ , effectively reducing  $f^\theta$  to a context-driven linear map. While this restricts  $F^\theta$  to a linear class, it remains sufficient for the discrete Gaussian settings considered here, as such transformations can exactly characterize the resulting Gaussian posteriors. Although more flexible architectures, such as Continuous Normalizing Flows (CNFs) (Chen et al., 2018), could be employed, we leave such generalizations for future work.

**Score network** To implement  $s^\theta$ , we construct a time-dependent MLP, where the time scalar  $t$  is embedded into a  $d_t$ -dimensional vector  $c_t$  as its Fourier features:  $c_t = [\sin(\omega_0 t), \dots, \sin(\omega_{d_t/2-1} t), \cos(\omega_0 t), \dots, \cos(\omega_{d_t/2-1} t)]$ , with the frequencies  $\omega_i = 2\pi \cdot 10^{\log_{10} \omega_{\min} + \frac{i}{d_t/2-1} (\log_{10} \omega_{\max} - \log_{10} \omega_{\min})}$ ,  $i = 0, 1, \dots, d_t/2 - 1$ , we choose  $\omega_{\min} = 0.001$ ,  $\omega_{\max} = 10$ , and  $d_t = 32$ . We also deploy the same embedding strategy to the edge length information  $T_v$ , obtaining the embedding  $c_T$ . The inputs to  $s^\theta$  are concatenated  $[c_t, z, \tilde{\mu}_v, c_T, c_v]$ , where  $\tilde{\mu}_v = H_v^{-1}\eta_v$ . Equation (17) is numerically integrated via the Euler-Maruyama scheme.

### B.2. Linear Gaussian model

To regulate the variance across leaf nodes, we set  $\alpha = 1 - 0.1^{\frac{1}{N_{\text{depth}}}}$ , ensuring that the total variance at depth  $N_{\text{depth}}$  remains bounded as  $\text{Var} = 1 - (1 - \alpha)^{N_{\text{depth}}} = 1 - 0.1 = 0.9$ , independent of  $N_{\text{depth}}$  grows. Synthetic observations for all leaf nodes are fixed at zero, with an associated observation noise covariance of  $\Sigma_{\text{obs}} = 10^{-3}\mathbf{I}$ . The RealNVP  $F^\theta$  is

configured with four affine coupling layers using SiLU activations, with hidden dimensions consistently set to  $4d$ , where  $d$  denotes the state dimensionality. Optimization is performed using the Adam optimizer with a learning rate of  $10^{-3}$  over 5,000 iterations. For the Monte Carlo estimation, a sample size of 50 is maintained across all experiments.

We further evaluate the proposed subsampling technique, as detailed in Theorem 4.4, by analyzing the resulting training loss trajectories. For this experiment, we configure a balanced tree with  $d = 2$ ,  $N_{\text{depth}} = 4$ ,  $N_{\text{branch}} = 3$ . Synthetic observations are fixed at zero with an observation covariance of  $\Sigma_{\text{obs}} = 10^{-3}\mathbf{I}$ , and selected leaves are sampled uniformly during training. Figure 5a illustrates the negative ELBO (NELBO) trajectories both with and without importance sampling. While the raw loss curve with subsampling (light blue) exhibits significantly higher variance compared to the non-subsampling baseline (orange), the moving average (dark blue) successfully converges to the analytical lower bound provided by the RTS smoother. This increased stochasticity represents a strategic trade-off for improved computational efficiency; in this configuration, the importance sampling approach achieved a speedup of over fourfold while maintaining convergence accuracy.

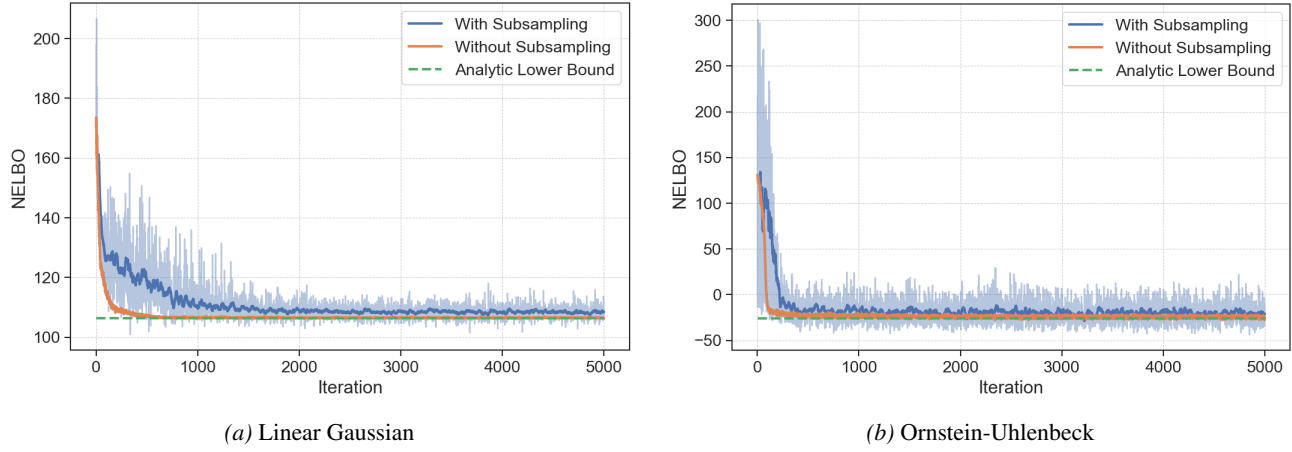


Figure 5. NELBO convergence with and without subsampling. Optimization trajectories are shown for: (a) Linear Gaussian model on a balanced tree and (b) Ornstein-Uhlenbeck process on an irregular tree. The dashed green line represents the analytical ground truth. While the raw subsampling estimator (light blue) exhibits higher stochasticity, its moving average (dark blue) consistently converges to the theoretical optimum alongside the full-tree baseline (orange).

### B.3. Ornstein-Uhlenbeck model

The considered SDE is specified with the parameters:  $\alpha = \begin{bmatrix} 4.0 & -1.0 \\ -2.0 & 1.0 \end{bmatrix}$ ,  $\Theta = \begin{bmatrix} 2.0 \\ -3.0 \end{bmatrix}$ , and  $\sigma = \begin{bmatrix} 0.2 & 0.0 \\ 0.0 & 0.1 \end{bmatrix}$ . This configuration ensures coupling between the two components of  $Z_v(t)$ , while assigning them distinct stationary means and evolutionary rates. The observations are made by adding noise with covariance  $\Sigma_{\text{obs}} = 10^{-3}\mathbf{I}$  on the leaf states of a forward unconditioned simulation. To numerically integrate the SDE along the edge, we deploy the Euler-Maruyama scheme with 50 discrete time steps.

To construct the random tree topology, we employ a stochastic generation process. At each step, a leaf is randomly selected to either bifurcate, incrementing the leaf count, or elongate, extending the lineage. This procedure continues until the pre-specified budget of 40 vertices is reached, resulting in a non-regular topology with varied internal degrees. The final tree, illustrated in Figure 6, comprises 13 leaves and a maximum depth of 13. The edge lengths are sampled from  $\mathcal{U}(0, 1)$ . This topology is particularly representative due to its structural asymmetry: the left subtree (rooted at vertex 1) is characterized by a deep structure with few leaves, whereas the right subtree (rooted at vertex 2) is shallower but possesses a higher leaf density. Given the amortized learning framework, the network must effectively reconcile information across both long-range dependencies and the complex aggregation of multiple observations. We also provide a summary of all vertex distributions as shown in Figure 7, where it can be seen that our method successfully recovers the exact posteriors across all the vertices.

The score network  $s_\theta$  is implemented as a 4-layer MLP with hidden dimensions of 64 and SiLU activations. Optimization is performed using the Adam optimizer with a learning rate of  $10^{-3}$  over 5,000 iterations, with the gradient norm clipped to 1.0. For the Monte Carlo estimation, a sample size of 50 is used. We further validate the subsampling technique in this continuous-time setting using a highly irregular tree topology. As illustrated in Figure 5b. The root-to-leaf paths in this

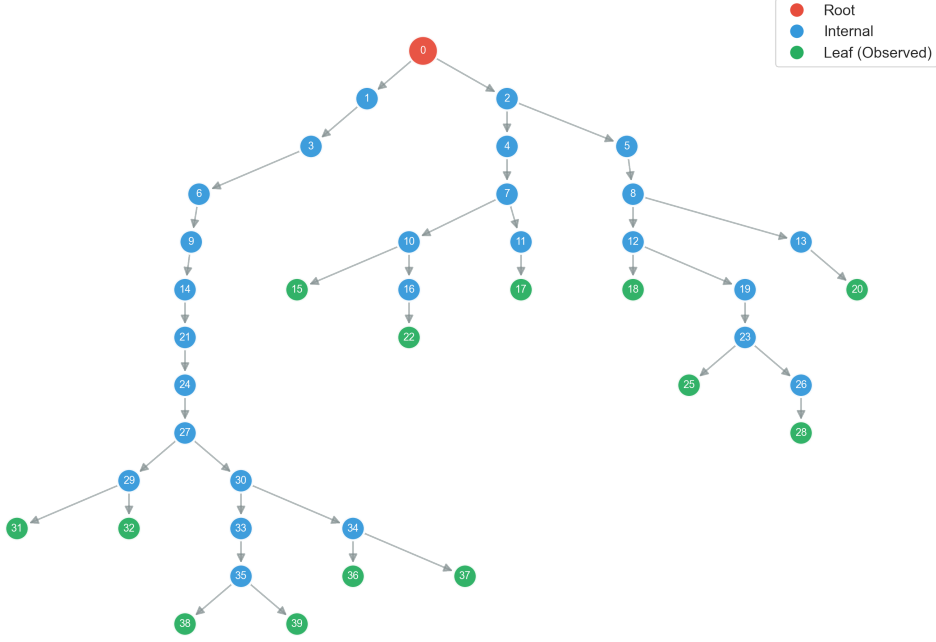


Figure 6. Topology of the tree generated with a stochastic branching process, with 40 vertices of which 13 are leaves. Numbers in vertices stand for global indices. The branch lengths are not indicated in the topology.

scenario possess varying lengths, unlike the uniform path lengths in the previous balanced tree example. This structural asymmetry complicates amortized learning and increases the variance of the loss during the training; nevertheless, the loss consistently converges to the analytical lower bound, confirming the robustness of importance sampling for irregular trees with continuous edge dynamics. In this specific example, we also observed over two times the training speed acceleration.

#### B.4. Double-well diffusion model

We set the parameters of double-well SDE as  $(\alpha, \sigma) = (3.0, 0.5)$  and the observation noise covariance as  $\Sigma_{\text{obs}} = 0.01$ . Combining with the trajectories visualization in Figure 3, we present the empirical marginal histograms of non-root vertices as Figure 8. In the absence of observation conditioning, the marginal distributions across all vertices remain symmetrically bimodal (see Figure 3 (a)). We break this symmetry by imposing asymmetric evidence at the leaves: the two top-subtree leaves are conditioned at  $+1$ , while the two bottom-subtree leaves are conditioned at  $-1$ . These opposing signals are intended to force the internal vertex distributions to collapse into unimodal states consistent with their descendants. As shown in Figure 8 (b), the uncorrected guided proposal fails to achieve clear mode separation at the internal layer. In contrast, the learned variational posterior matches the reference MCMC baseline in effectively distinguishing the modes, accurately reconstructing the unimodal internal vertex distributions (see Figure 8 (c), (d)).

We further evaluate the method in a configuration designed to induce a bimodal posterior by conditioning the leave on  $[-1, -1, -1, 1]^\top$ . Figure 9 highlights the issue of mode collapse inherent in the MCMC approach. As seen in panels (b) and (c), independent MCMC chains become trapped in isolated local equilibrium ( $\pm 1$ ) due to the high energy barrier between modes: Chain 1 locks onto a solution where the top branch (orange) commits to the positive well ( $+1$ ), while Chain 2 collapses to the negative well ( $-1$ ). Neither chain explores the full landscape. In contrast, our variational method (panel d) successfully learns the bimodal posterior, generating trajectories that cover both modes simultaneously. This capability is further confirmed by the histogram plots in Figure 10. At the critical branching time  $t = 4.0$  (left column), the variational distribution (d) correctly recovers the bimodal distribution for both lineages, whereas the individual MCMC chains (b, c) are restricted to single, narrow peaks. This demonstrates that our method can robustly resolve multimodality that typically challenges the MCMC method.

In this experiment, the score network  $s^\theta$  is implemented as a 5-layer MLP with hidden dimensions of 64 and SiLU activations.

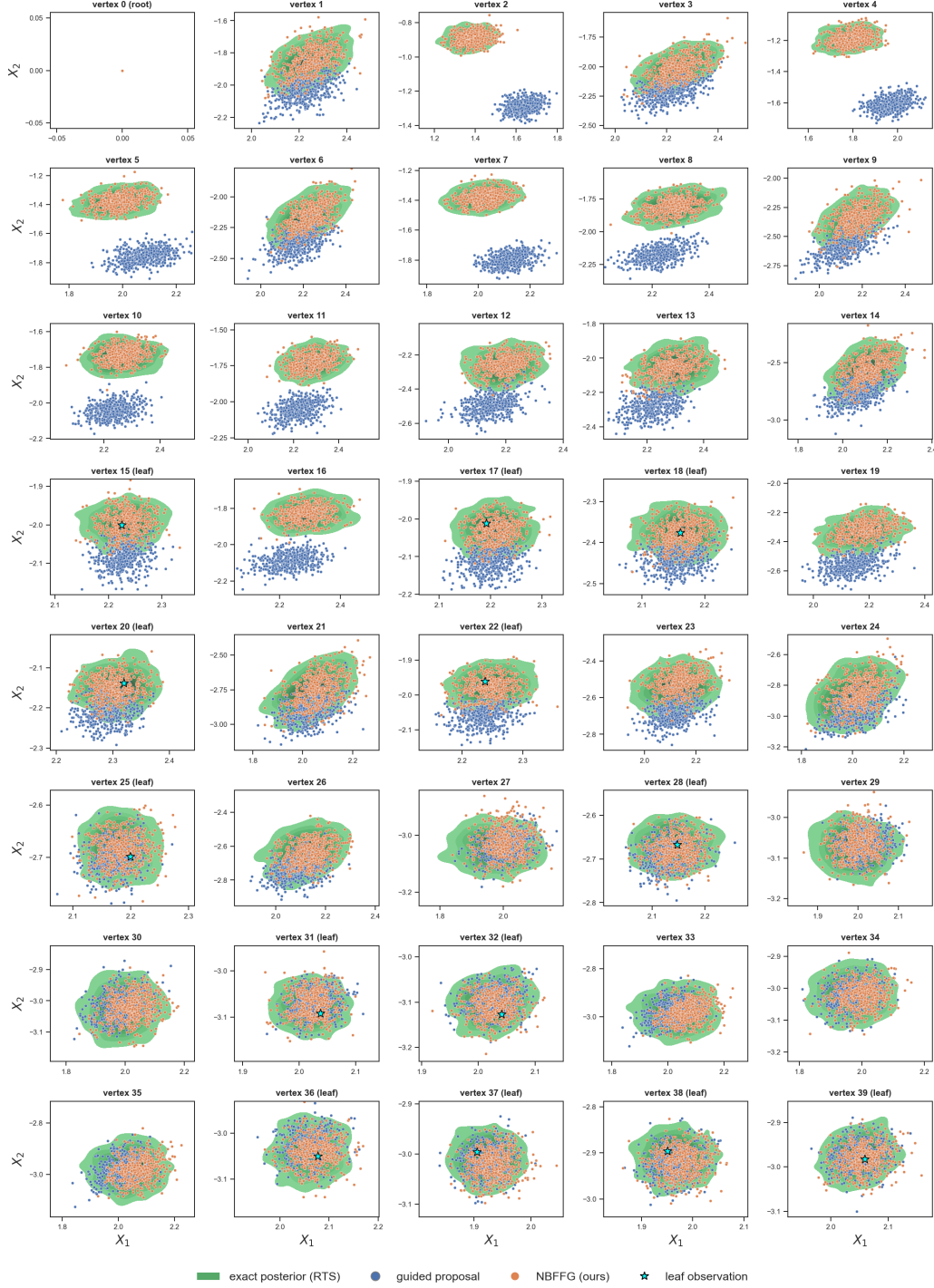


Figure 7. Empirical distributions of 500 independent samples of the guided proposal (gray) and the learned variational posterior (orange) against the analytical ground truth (RTS, green contours) across all vertices on the tree. The vertex ID corresponds to the numbers indicated in the tree topology Figure 6.

Optimization is performed using the Adam optimizer with a learning rate of  $10^{-3}$  over 10,000 iterations, with the gradient norm clipped to 1.0. Since the process is highly non-linear, we deploy a finer time discretization with 200 steps per edge. The auxiliary process is chosen as a standard Brownian motion with  $B = \beta = 0$ , and  $\tilde{\sigma} = \sigma$ . We also use the importance sampling techniques during the training. For the Monte Carlo estimation, a sample size of 50 is used.

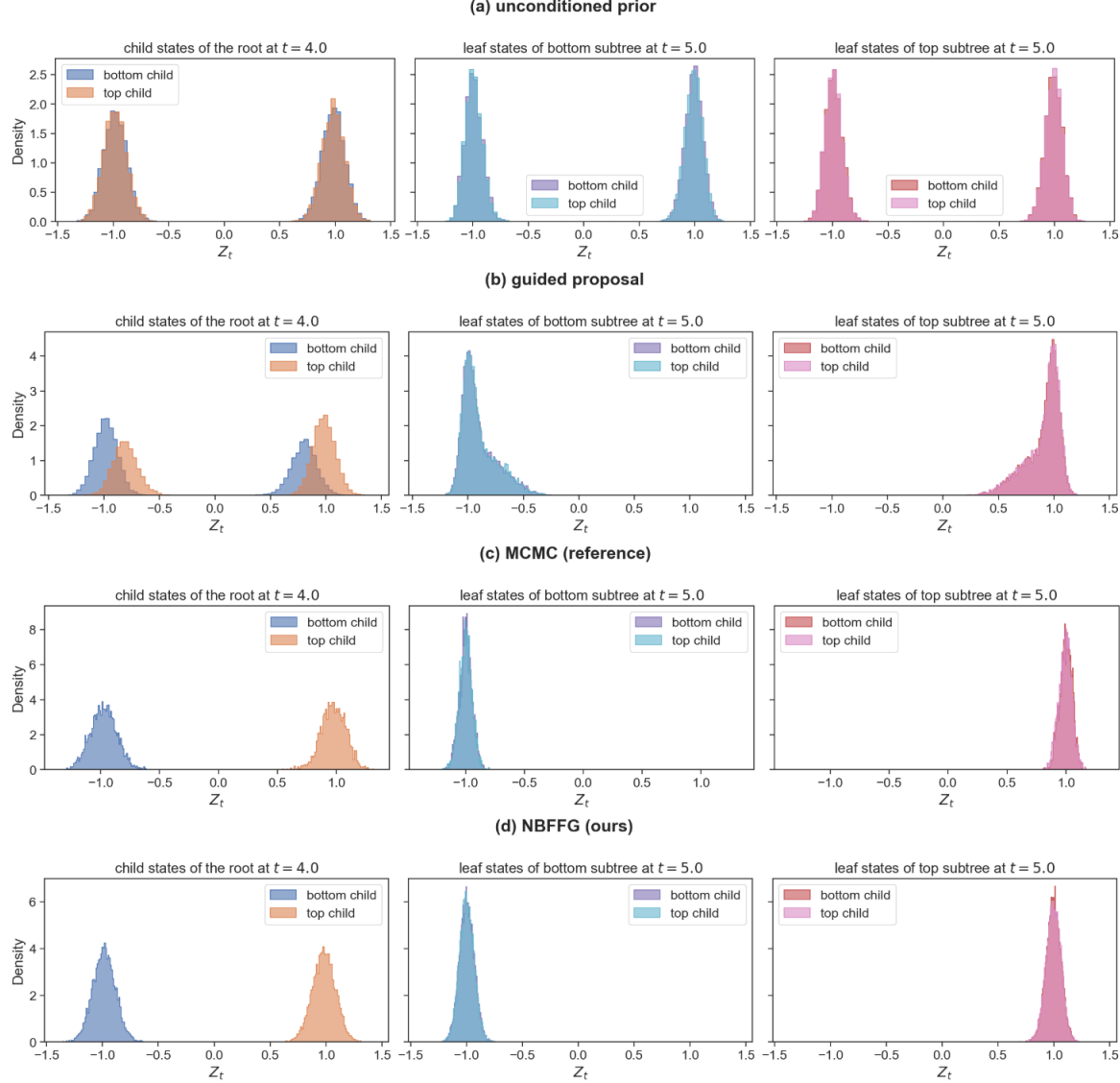


Figure 8. Empirical state distributions across tree nodes for the double-well potential when conditioning on  $[-1, -1, 1, 1]^\top$ . Histograms are made up of 10,000 samples at times corresponding to the topological levels. (a) the unconditioned prior process; (b) the raw guided proposal; (c) the guided proposal corrected by MCMC sampling; (d) the learned variational posterior. Colors shared with the trajectory visualization Figure 3 identify the samples from corresponding edges.

### B.5. Stochastic phylogenetic shape evolution

We consider the outline of butterfly wings represented by point configurations  $z = (z^1, \dots, z^n)$ ,  $z^i \in \mathbb{R}^2$  called *landmarks*. At time  $t$ , the outline of the butterfly shape  $Z(t) = z$  follow the Kunita flow SDE:

$$dZ(t)^i = \int_{\mathbb{R}^2} \kappa(Z(t)^i, \zeta) dW_t(\zeta) d\zeta, \quad (48)$$

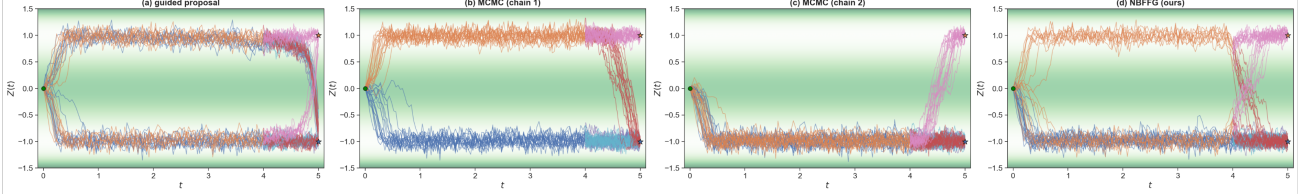


Figure 9. Visualization of double-well diffusion conditioned on the leaf observation  $[-1, -1, -1, 1]^\top$  on a binary tree. The figure displays 20 samples from (a) the raw guided proposal; (b) one chain of MCMC samples corrected from the guided proposal; (c) another independent chain of MCMC samples, and (d) the learned variational posterior. Green dots at  $t = 0.0$  represent the root, and stars at  $t = 5.0$  represent the observed values  $\pm 1$  at the leaf nodes. The background green shading illustrates the potential wells.

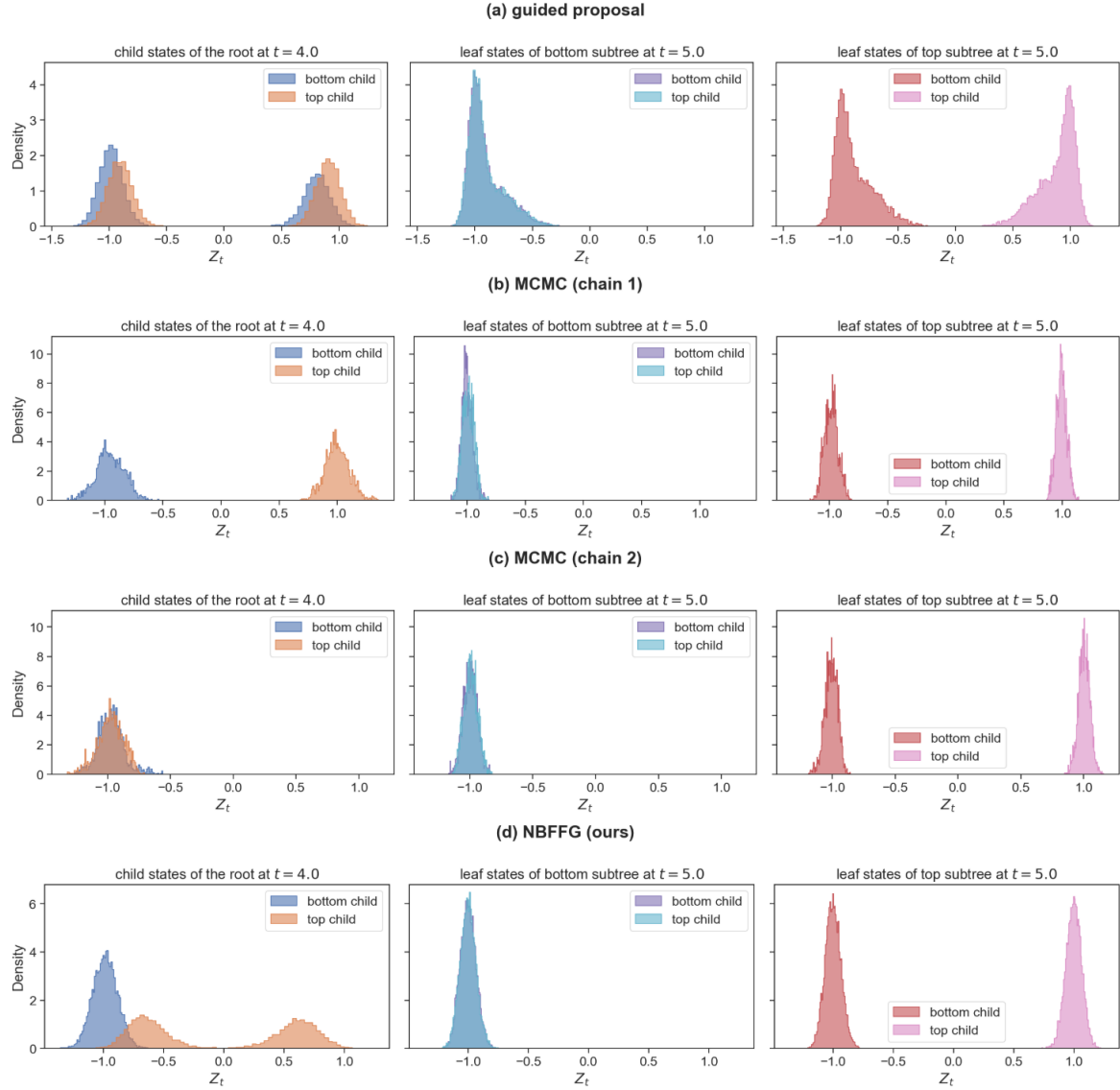


Figure 10. Empirical state distributions across tree nodes for the double-well potential when conditioning on  $[-1, -1, -1, 1]^\top$ . Histograms are made up of 10,000 samples at times corresponding to the topological levels. ((a) the raw guided proposal; (b) one chain of MCMC samples corrected from the guided proposal; (c) another independent chain of MCMC samples, and (d) the learned variational posterior. Colors shared with the trajectory visualization Figure 9 identify the samples from corresponding edges.

where  $\kappa$  is a kernel that describes the diffusivity operator of the Kunita flow in integral form. We simplify this infinite-dimensional model by considering its finite-dimensional version:

$$dZ(t) = K(Z(t))dW_t, \quad (49)$$

where  $K$  is the matrix  $[K(z)]_{ij} = \kappa(z^i, z^j)\mathbf{I}_2$ , and  $W$  is an  $2n$ -dimensional Wiener process. We take the kernel  $\kappa(z^i, z^j) = \bar{\kappa}(\|z^i - z^j\|)$ , where  $\bar{\kappa}(r) = 4\alpha(3 + 3r + r^2)\exp(-r/\sigma)$ , and select the kernel parameters  $\alpha = 0.05, \sigma = 0.2$ . For the auxiliary process, we redefined  $\tilde{\sigma}$  iteratively as the backward filtering processing from leaves to root. Along the edge  $(\text{pa}(v), v)$ ,  $\tilde{\sigma}(t) = \tilde{\sigma} = K(H_v^{-1}\eta_v)$ , i.e., the evaluation of  $K$  on the child approximate mean  $H_v^{-1}\eta_v$ .

To infer the root posterior, we assign a fixed virtual root prior to the actual root to be estimated. The fixed value of the virtual root is the Euclidean mean of the leaf landmarks' coordinates, and the edge length is set to be the mean of all the other existing edges. We collected 118 landmarks for each butterfly species, which were subsequently downsampled to 59 points. Landmark coordinates were normalized to the range  $[-1, 1] \times [-1, 1]$ , and branch lengths were scaled such that the maximum total path length equals 1.0. We assign observation noise covariance of  $\Sigma_{\text{obs}} = 0.05^2\mathbf{I}$ . The score network  $s_\theta$  is implemented as a 6-layer MLP with hidden dimensions of 1024 and SiLU activation functions. Optimization was performed using the Adam optimizer with a learning rate of  $1e-4$  over 5,000 iterations. To facilitate numerical integration, each edge was discretized into 10 equal intervals to establish the time grids. To estimate the expectation, we simulate 10 independent trajectories along each edge.

Figure 11 shows that our method is able to successfully reconstruct coherent shapes across all ancestral lineages. As an interesting observation, we see that the posterior mean occasionally has less sharp features in certain extant species (e.g., *P. thoas* or *P. antimachus*). We attribute this to two primary factors. First, the inference process inherently balances conflicting signals from the diverse population; when conditioning on a mix of species with and without tails (e.g., *P. cresphontes* vs. *P. deiphobus*), the posterior mixes both signals. Second, the kernel correlation scale ( $\sigma = 0.2$ ) enforces strong local smoothness. While this constraint is crucial for preserving valid wing topology (preventing self-intersection or jaggedness), it can limit the independent movement of adjacent landmarks, making it difficult to capture fine details like sharp tail extensions. Future work could address this via spatially adaptive kernels (e.g., assigning a lower  $\sigma$  to tail regions), and one could test a model based on this to see which model is most likely for the observed data.

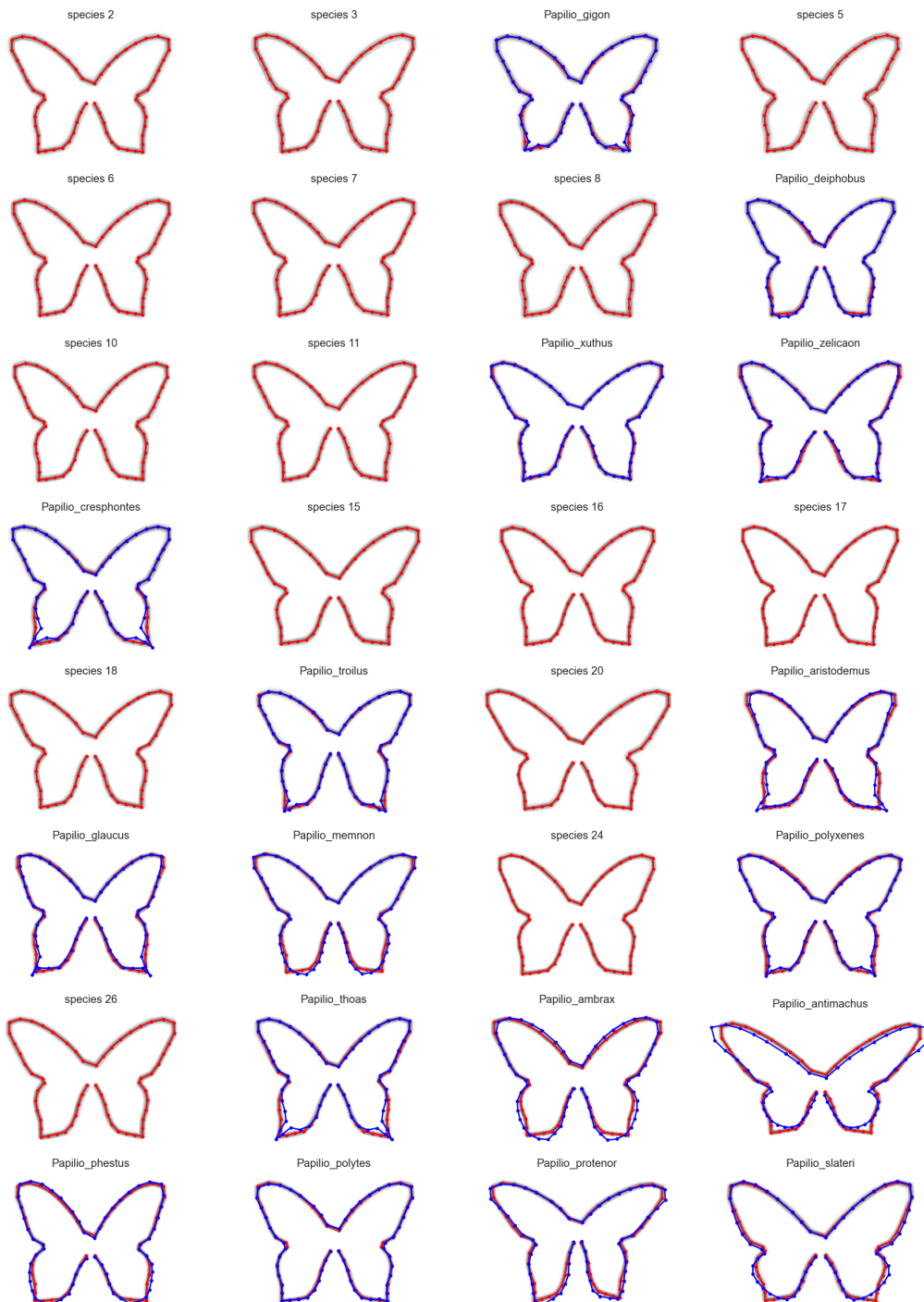


Figure 11. Posterior morphological distributions across the *Papilio* phylogenetic tree. The figure displays posterior shape samples for all internal nodes and extant species. For each node, 100 independent posterior samples are visualized as semi-transparent gray curves, with their corresponding empirical means highlighted in red. Extant leaf species are distinguished by blue outlines representing the ground-truth observed morphology. The visualization illustrates the model’s ability to capture morphological uncertainty while accurately reconstructing ancestral states.